RIVISTA DEL NUOVO CIMENTO Vol. 41, N. 11 2018

The physics of earthquakes from space gravity missions

R. Sabadini and G. Cambiotti

Department of Earth Sciences, University of Milano - Milano, Italy

received 20 May 2018

Summary. — Developments in the physical modelling of the Earth's interior and space geodesy make it possible nowadays to exploit the gravity signature and deformation patterns, including their time variations, caused by megathrust earthquakes at subduction zones with moment magnitude M_w higher than 9.0, as the 2004 Sumatran and 2011 Tohoku-Oki ones. In order to achieve these goals, it has been necessary to develop realistic self-gravitating, compressible Earth's models, stratified in terms of density and rheological properties of the Earth's interior. This new class of models allows us to comprehend some not yet fully appreciated mathematical aspects of viscous stress relaxation, such as the interplay between discrete and continuous relaxation spectra depending on the style of density stratification of the viscoelastic mantle or the effects on the gravity fields of sometimes used simplified treatments of compressibility. We show how GRACE and GOCE data allow us to invert for the mass redistribution, inner volume variations, gravity perturbations and surface deformation affecting areas and volumes larger than those embedding the gouge of the earthquakes, including the slip distribution over the fault surface. A correct interpretation of the mass redistribution process for megathrust earthquakes is important for the understanding of the physics of the ocean and Solid Earth coupling, causing the tsunami which struck Sumatra and Thailand and the eastern coast of Japan due to the huge amount of water washed out from the epicentral region as seen from GRACE data and physical modelling. In the present study we focus on the physics of the co-seismic and post-seismic gravity changes due to a $M_w = 7.0$ scenario normal-fault earthquake, comparable to the 1980 Irpinia earthquake. Our modelling provides the earthquake gravity effects within the perspective of the upcoming Next Generation Gravity Missions (NGGM), designed to detect the gravity anomalies caused by earthquake magnitudes as low as $M_w = 7$ as well as the gravity anomalies due to the active tectonic processes responsible for the earthquakes. It is expected that the time-dependent gravity will be exploited at the GOCE spatial resolution and at GRACE time resolution, or even better, thanks to a new class of payload instrumentation, based on a laser ranging system measuring the distance variation between one or two pairs of satellites flying in formation at altitudes of about 300 km and at about 100 km separation, each satellite differently affected by the gravity changes of our Planet.

1. – Introduction

Geophysical processes occurring within the Earth involve both particle displacements and gravity changes, the latter caused by displacements of interfaces separating material of different density or by volume changes due to compression or dilatation of the material: the joint use of Earth's mathematical models capable of simulating the physical processes and of space geodetic data, sampling displacements and gravity changes, allows nowadays to constrain the physics of the Earth's interior. This work is devoted to the exploitation of some issues pertaining to global Earth's model, some technical details of which have not received adequate attention in the international literature and to the presentation of preliminary results on the gravitational effects of earthquakes which the Next Generation Gravity Missions (NGGM) [1] have the potential to disclose, improving substantially our knowledge on the physics of the seismic cycle with respect to what we learnt from GRACE (Gravity Recovery And Climatological Experiment) and GOCE (Gravity and steady state Ocean Circulation Explorer) space gravity missions. Among the various processes affecting our Planet, we choose herein to focus on the earthquakes, since they represent a major aspect of Plate Tectonics, an important aspect of which stands on the slow but continuous relative motion and deformation of the tectonic plates ending into abrupt, catastrophic ruptures in the outer shell of the Earth. The earthquake is a perfect example of a geophysical process involving both displacements and gravity changes, because it displaces the crustal material in the near and in the far field with respect to the fault and produces at the same time changes in the gravity, due to the displacement of material of varying density and because it causes compression and dilatation of the Earth's material, so augmenting and diminishing the density of the material at different depths. Nowadays, displacements caused by earthquakes at the Earth's surface are recorded by GNSS (Global Navigation Satellite System) and SAR (Synthetic Aperture Radar) while gravity changes are recorded by GRACE, but limited to magnitudes higher than $M_w = 8.5$.

In order to tackle self-consistently the modelling of earthquakes of different magnitudes, including those as the 2004 Sumatran, $M_w = 9.3$ or the 2011 Tohoku-Oki ones, $M_w = 9.1$, which broke the Earth's crust with faults whose dimension parallel to the Earth's surface is of the order of 10^2–10^3 km, we need spherical and self-gravitating

Earth's models, whose physics is exploited in sects. **2** and **3**: for fault dimensions of some hundreds kilometres the effects of sphericity are in fact not negligible and, besides, a correct treatment of the central gravity field requires not only a spherical model but also a self-gravitating one, meaning with this wording that our Earth's model must account for the effects of the perturbation of the gravitational field once the Earth is deformed or masses are displaced within the Earth or at its surface. In the forthcoming sect. **2** we deal with some detailed aspects of this class of models, as those associated with compressibility and density stratification, within the framework of spherical, self-gravitating, stratified and viscoelastic Earth's models: it should be noted that in their characterization we added the viscoelasticity, since when dealing with the earthquakes our modelling must account for the instantaneous elastic deformation plus for the viscoelastic effects, due to the fluid-like, viscous behaviour of the deep portions of the Earth. Furthermore, the model must be stratified, in terms of density, elastic and viscoelastic parameters, in order to match the in-depth mechanical properties of our Planet, as we learnt from decades of its seismological exploration and Post Glacial Rebound studies. Section **4** is devoted to the presentation of the new technology, based on laser tracking between satellites, opening new perspectives in the detection of the gravity changes with high accuracy in time and at high spatial resolution. Sections **5** and **6** are devoted to the analysis of the gravitational effects of earthquakes of different magnitudes, from magnitude $M_w = 7$ to magnitude $M_w = 9$, and normal fault or thrust earthquakes, the former caused by the extension of the crust, as for the case of the $M_w = 6$–7 earthquakes in the Apennines and the latter caused by the compression of the plates, as for the case of the giant, around $M_w = 9$, Sumatran and Tohoku-Oki earthquakes. The gravitational effects will be exploited in terms of their amplitude variations, in micro-Gal (μGal) for the gravity and in terms of their characteristic wavelength of the gravity signal.

2. – Spherical, self-gravitating, viscoelastic, compressible Earth's models

The mathematics described in sects. **2-3**, based on [2], displays the response of a spherical, self-gravitating and compressible Earth model to external forces and loads seated at its surface or at its interior, as well as to earthquake faults, the topic of this work. Readers willing to catch all the technical details of viscoelastic relaxation theory may refer to chapters 1 and 2 of [2]: we discuss herein some basic physics of the momentum and Poisson equations, relevant in viscoelasticity, skipping all the steps leading to the viscoelastic solution of the system of linear differential equations obtained by expanding in spherical coordinates the momentum and Poisson equations, whose solution is discussed in terms of the structure of our Planet, depending on its mechanical, density and rheological stratification.

As stated in the Introduction, we are interested in both co-seismic and post-seismic gravity signals from earthquakes, which means that we have to choose the rheological law relating stress to strain and strain rate and thus describing how the Earth's material reacts to applied stresses, instantaneously or elastically when dealing with co-seismic gravity signals, or over time, when dealing with post-seismic signals; we will not deal with non-linear rheological laws or finite-strain theory, since for a wide spectrum of Solid Earth relaxation processes, such as co- and post-seismic deformations, both can be neglected.

2˙1. *Viscoelastic rheology and correspondence principle.* – The simplest viscoelastic model describing the Earth as an elastic body for short time scales and as a viscous fluid for time scales characteristic of post-seismic deformation, the focus of the present work aimed at detecting this seismic phase via gravity anomalies from space missions, is the linear Maxwell solid, whose one-dimensional mechanical analog is given by a spring and a dashpot, depending, respectively, on the rigidity μ and on the viscosity ν. The speed for shear wave propagation depends on the square root of the instantaneous rigidity μ, as well as the co-seismic deformation and co-seismic gravity changes depend on the rigidity, whereas the strength of post-seismic deformation rates and post-seismic gravity rate of change depend on the magnitude of the steady-state viscosity ν. Rigidities and viscosities are obtained, respectively, from seismology and from Post Glacial Rebound or post-seismic deformation studies.

We assume linear and isotropic constitutive equations, relating stress and strain; perturbations are isentropic and isochemical because viscoelastic relaxation processes, as co- and post-seismic ones, occur on time scales shorter than those characterizing heat diffusion and changes in the chemical composition of the rocks. The Maxwell rheology is defined by the following constitutive equations:

$$\boldsymbol{\sigma}^{\delta} = \kappa\,\Delta\,\mathbf{1} + 2\,q \star \partial_t \boldsymbol{\epsilon}_D, \tag{1}$$

where $\boldsymbol{\sigma}^{\delta}$ denotes the incremental Cauchy stress tensor and $\boldsymbol{\epsilon}_D$ denotes the deviatoric strain tensor; ∂_t and $\star$ stand for the partial derivative with respect to time t and for the time convolution

$$\left(q \star \partial_t \boldsymbol{\epsilon}_D\right)(t) = \int_0^t q(t-t')\,\partial_{t'}\boldsymbol{\epsilon}_D(t')\,\mathrm{d}t', \tag{2}$$

where κ, q and $\boldsymbol{\epsilon}_D$ are the adiabatic bulk modulus, the shear relaxation function and the deviatoric strain tensor

$$\boldsymbol{\epsilon}_D = \boldsymbol{\epsilon} - \frac{\Delta}{3}\,\mathbf{1}. \tag{3}$$

In this respect, the first and second terms on the RHS of eq. (1) describe the isotropic and deviatoric material incremental stresses, with the divergence $\Delta = \boldsymbol{\nabla}\cdot\boldsymbol{u}$, where $\boldsymbol{u}$ denotes the displacement of the particle; the factor $\kappa\,\Delta$ multiplying the identity matrix $\mathbf{1}$ corresponds to the negative of the material incremental pressure

$$p^{\delta} = -\kappa\,\Delta, \tag{4}$$

as shown by comparison of eq. (1) and eq. (34).

For the Maxwell solid, the shear relaxation function takes the following form:

$$q(t) = \begin{cases} \mu \exp\left(-\dfrac{t}{\tau}\right), & t \geq 0, \\ 0, & t < 0, \end{cases} \tag{5}$$

where τ is the Maxwell time defined by the ratio between the viscosity ν and the shear modulus μ

$$\tau = \frac{\nu}{\mu}\,. \tag{6}$$

The shear modulus values as a function of depth are well constrained from seismology and wave propagation, while the viscosity values are subject to uncertainties, for the obvious reason that, while for the shear modulus we can rely on a large number of seismological data from earthquakes, for viscosity estimates we must rely on Post Glacial Rebound or post-seismic deformation studies, the former representing a single event for our Planet, which ended about 7×10^3 yr ago, and the latter representing events which started to be studied recently, as we show hereinafter, and still requiring good quality data, as in fact the next generation gravity mission is expected to provide. In any case, Post Glacial Rebound studies constrain the upper mantle viscosity in the range 0.5×10^{20}–10^{21} Pa s, the lower mantle viscosity in the range 10^{22}–10^{23} Pa s and post-seismic studies indicate asthenospheric or intra-crustal viscosities in the range 0.5×10^{18}–10^{19} Pa s. The shear modulus range is 10^{10}–10^{11} Pa for our Planet: from these values for the viscosity and for the shear modulus, it is possible to estimate the Maxwell times for the Maxwell rheology. We should point out that, while the Maxwell time characterizes the rheological law, it is necessary to solve the coupled momentum and Poisson equations as described in the following in order to quantify the characteristic relaxation times, associated to the modes triggered by the surface and internal density and mechanical discontinuities, which determine the evolution in time of the Earth and of its internal portions once perturbed by any kind of forcing.

The Maxwell rheology describes the transition from the elastic to the Newtonian fluid behaviour of the Earth occurring on the time scale given by the Maxwell time τ. Although the constitutive equations of both elastic and Newtonian fluid bodies relate stress at a given time to only strain and strain rate at that time, eqs. (1) and (2) show that for the Maxwell rheology the viscoelastic stress at a given time depends on the whole strain rate history before that time, as shown by the convolution above.

The Maxwell rheology does not account for bulk relaxation because we assume that the adiabatic bulk modulus κ is constant, which is consistent with reality. The bulk modulus is defined starting from the differential form of the density state function $\rho(p, s, c)$ that describes the density of a particle as function of its pressure p, entropy s and chemical composition c,

$$\mathrm{d}\rho = \left.\frac{\partial\rho}{\partial p}\right|_{s,c} \mathrm{d}p + \left.\frac{\partial\rho}{\partial s}\right|_{p,c} \mathrm{d}s + \left.\frac{\partial\rho}{\partial c}\right|_{p,s} \mathrm{d}c. \tag{7}$$

We choose the entropy as thermodynamic quantity rather than the temperature since we consider isentropic perturbations. The differentials $\mathrm{d}\rho$, $\mathrm{d}p$, $\mathrm{d}s$ and $\mathrm{d}c$ denote the perturbations with respect to the initial state of the particle, and they correspond to the material incremental fields ρ^δ, p^δ, s^δ and c^δ.

Within the assumption of isentropic and isochemical perturbations, or $s^\delta = 0$ and $c^\delta = 0$, we obtain

$$\rho^\delta = \left.\frac{\partial\rho}{\partial p}\right|_{s_0,c_0} p^\delta, \tag{8}$$

where the subscript 0 denotes the initial fields. By making use of the material incremental density $\rho^\delta = -\rho_0\,\Delta$ (see also eq. (43)) and of eq. (4) into eq. (8), we obtain the definition of the adiabatic bulk modulus κ entering the constitutive equation (1) in terms of the partial derivative of the density with respect to the pressure in the initial state

$$\frac{\rho_0}{\kappa} = \left.\frac{\partial \rho}{\partial p}\right|_{s_0,c_0}. \tag{9}$$

A powerful tool for solving transient problems of linear viscoelasticity is the Correspondence Principle, based on the result that the viscoelastic problem in the Laplace domain is formally identical to the elastic problem in the time domain, as shown hereinafter.

The Laplace transform of a function $f(t)$ is formally defined as

$$\mathcal{L}[f] = \int_0^\infty f(t) e^{-st} \mathrm{d}t, \tag{10}$$

with $\mathcal{L}$, t and s being the Laplace transform operator, time and Laplace variable (which has dimension of inverse time). Introducing $\tilde{f}(s) = \mathcal{L}[f]$, it is straightforward to show that the Laplace transform of the time derivative of the function $f(t)$ yields

$$\mathcal{L}[\partial_t f] = s\,\tilde{f}(s) - f(0) \tag{11}$$

and that the Laplace transform of the time convolution of two functions $f(t)$ and $h(t)$ yields the product of the Laplace transforms $\tilde{f}(s)$ and $\tilde{h}(s)$

$$\mathcal{L}[f \star h] = \tilde{f}(s)\,\tilde{h}(s), \tag{12}$$

with $\star$ denoting the time convolution operator.

In the following mathematical developments we will consider the most general external forcing, surface or internal loading and earthquakes that act on the Earth starting immediately after the initial time, namely at $t = 0^+$, and we restrict our attention on right-handed functions that differ from zero only for $t > 0$

$$f_+(t) = f(t)\,H(t - 0^+). \tag{13}$$

Here $H(t)$ is the Heaviside function.

The Laplace transform of the right-handed function $f_+(t)$ is the same as the original function $f(t)$

$$\tilde{f}_+(s) = \tilde{f}(s), \tag{14}$$

while the Laplace transform of its derivative yields

$$\mathcal{L}[\partial_t f_+(t)] = s\,\tilde{f}(s), \tag{15}$$

because the second term on the RHS of eq. (11) disappears due to the step-like discontinuity of $f_+(t)$ at $t = 0^+$. From now on, we intend time-dependent functions describing

forcings and perturbations as right-handed functions, even though the subscript + will be omitted.

By making use of eq. (15), the Laplace transform of the constitutive equation for the Maxwell solid, eq. (1), yields

$$\tilde{\boldsymbol{\sigma}}^{\delta}(s) = \kappa\, \tilde{\Delta}(s)\, \mathbf{1} + 2\, \hat{\mu}(s)\, \tilde{\boldsymbol{\epsilon}}_D(s), \tag{16}$$

with $\hat{\mu}(s)$ being the following function of the Laplace variable s:

$$\hat{\mu}(s) = \frac{\mu\, s}{s + \frac{1}{\tau}}\,. \tag{17}$$

Note that eq. (16) has the same form as Hooke's law for linear elastic solids

$$\boldsymbol{\sigma}^{\delta} = \kappa\, \Delta\, \mathbf{1} + 2\, \mu\, \boldsymbol{\epsilon}_D, \tag{18}$$

where $\hat{\mu}(s)$ and the Laplace transforms of the fields are replaced by the shear modulus μ and the same fields in the time domain; we can thus derive the equations for viscoelastic bodies in the Laplace domain from elastic body equations. Particularly, after Laplace transformation, the momentum and Poisson equations for the viscoelastic body are formally equivalent to those for the elastic solid. We thus solve the equivalent elastic problem in the Laplace domain and, only at the last stage, we will perform the inverse Laplace transform of the solution to obtain the viscoelastic solution in the time domain. In this respect, we will also refer to the viscoelastic solution in the Laplace domain as the associated elastic solution.

The so-called Correspondence Principle states that the time-dependent viscoelastic solution of the momentum and Poisson equations can be found in a unique way from the inverse Laplace transformation of the associated elastic solution. In light of this analogy between the elastic and viscoelastic problems, afterwards we will omit the tilde to denote Laplace transforms and we do not distinguish between the shear modulus μ and the function $\hat{\mu}(s)$, eq. (17). In this respect, the following results can be seen both as the solution of the elastic static problem and the associated elastic solution for viscoelasticity.

2˙2. *Momentum and Poisson equations.* – For long time scale processes the inertial forces vanish and the conservation of linear momentum requires that the body force $\mathbf{F}$ per unit volume acting on the infinitesimal element of the continuum body is balanced by the stress acting on the surface of the element. At any time t, we have for the Cauchy stress tensor $\boldsymbol{\sigma}$ acting on the infinitesimal element

$$\boldsymbol{\nabla} \cdot \boldsymbol{\sigma} + \mathbf{F} = \mathbf{0}, \tag{19}$$

describing the momentum equation to be solved within the whole volume of the Earth.

The body force $\mathbf{F}$ accounts for the gravitation generated by the Earth, for internal and surface loads, and for external bodies responsible for tidal forces. It accounts also for all kinds of other contributions like centrifugal and seismic forces. We decompose the body force $\mathbf{F}$ into a non-conservative force $\mathbf{M}$ representing the equivalent body force for shear dislocations and a conservative force in terms of the gradient of the potential ϕ

$$\mathbf{F} = \mathbf{M} - \left(\rho + \rho^L\right) \boldsymbol{\nabla}\phi, \tag{20}$$

where ρ and ρ^L are the densities of the Earth and loads, and the potential ϕ consists of the gravitational potentials of the Earth, ϕ^E, loads, ϕ^L, tidal, ϕ^T, and centrifugal, ϕ^C. Each term in these equations has the dimension of $\mathrm{N/m^3}$, or force per unitary volume,

$$\phi = \phi^E + \phi^L + \phi^T + \phi^C. \tag{21}$$

The gravitational potentials ϕ^E and ϕ^L are due to the density of the Earth ρ and loads ρ^L, while the tidal potential is due to the density of external bodies ρ^T. They satisfy the following Poisson equations:

$$\nabla^2\phi^E = 4\,\pi\,G\,\rho, \tag{22}$$

$$\nabla^2\phi^L = 4\,\pi\,G\,\rho^L, \tag{23}$$

$$\nabla^2\phi^T = 4\,\pi\,G\,\rho^T, \tag{24}$$

where G is the universal gravitational constant. Note that the density ρ^T of external bodies, responsible for the tidal potential ϕ^T, does not enter the momentum equation (19) via eq. (20) because, by definition, external bodies do not load the Earth, *i.e.*, the balance of forces acting on external bodies does not involve surface forces from the Earth. The centrifugal potential ϕ^C due to the Earth's rotation is defined as

$$\phi^C = \frac{1}{2}\,\left[(\boldsymbol{\omega}\cdot\boldsymbol{r})^2 - \omega^2\,r^2\right], \tag{25}$$

where $\boldsymbol{\omega}$ and $\boldsymbol{r}$ are the angular velocity of the Earth and the position vector, and $\omega = |\boldsymbol{\omega}|$ and $r = |\boldsymbol{r}|$ are the rotation rate and the radial distance from the Earth's centre.

The potential ϕ solves the Poisson equation

$$\nabla^2\phi = 4\,\pi\,G\,\left(\rho + \rho^L + \rho^T\right) - 2\,\omega^2, \tag{26}$$

where the latter term on the right-hand side (RHS) results from the Laplacian of the centrifugal potential $\nabla^2\phi^C = -2\,\omega^2$. Differently from the momentum equation (19), solved only within the volume of the Earth, the Poisson equation (26) is solved also outside the Earth.

Within the Lagrangian approach, the deformed Earth is described in terms of displacements of the particles of the continuum body,

$$\boldsymbol{r} = \boldsymbol{x} + \boldsymbol{u}(\boldsymbol{x}, t), \tag{27}$$

where t is the time, and $\boldsymbol{x}$ and $\boldsymbol{r}$ denote the initial and current positions of the particle subjected to the displacement $\boldsymbol{u}$. Following [3], we introduce the decomposition of scalar, vector and tensor fields into initial fields, (*i.e.*, the fields at the initial time), and local and material incremental fields,

$$f(\boldsymbol{r}, t) = f_0(\boldsymbol{r}) + f^{\Delta}(\boldsymbol{r}, t), \tag{28}$$

$$f(\boldsymbol{r}, t) = f_0(\boldsymbol{x}) + f^{\delta}(\boldsymbol{x}, t), \tag{29}$$

where f stands for the generic field. The initial field f_0 is denoted by the subscript 0 and describes the initial state of the undeformed Earth. The local incremental field f^{Δ}

is denoted by the superscript Δ and represents the increment of the field at point $\boldsymbol{r}$ with respect to the initial field at the same position $\boldsymbol{r}$. The material incremental field f^δ is denoted by the superscript δ and represents the increment of the field at point $\boldsymbol{r}$ with respect to the initial field at point $\boldsymbol{x}$, denoting the initial position of the particle currently located at $\boldsymbol{r}$, eq. (27).

Local and material incremental fields differ for the so-called advective incremental field, which is the difference between the initial field evaluated at the current and at the initial positions of the particle. Within the assumption of infinitesimal deformations, this difference is a first-order term that cannot be neglected,

$$f^\delta = f^\Delta + \boldsymbol{u} \cdot \boldsymbol{\nabla} f_0. \tag{30}$$

This relation holds both in the Lagrangian and Eulerian formulations, where the incremental fields are functions of the initial and current positions of the particle, because differences among incremental fields are of the second order and can be neglected.

Because the undeformed Earth is in non-rotating hydrostatic equilibrium, the initial potential ϕ_0 is the gravitational potential due to the initial density ρ_0 representing the density of the undeformed Earth, and satisfies the Poisson equation

$$\nabla^2 \phi_0 = 4\,\pi\,G\,\rho_0. \tag{31}$$

The initial Cauchy stress tensor $\boldsymbol{\sigma}_0$ is the initial hydrostatic stress

$$\boldsymbol{\sigma}_0 = -p_0\,\mathbf{1}, \tag{32}$$

where $\mathbf{1}$ and p_0 are the identity matrix and the initial hydrostatic pressure, entering with the minus sign according to the convention that stress is positive when it acts in the same direction as the outward normal to the surface. From the momentum equation at the initial time, the condition of non-rotating hydrostatic equilibrium is expressed as

$$-\boldsymbol{\nabla} p_0 - \rho_0\,\boldsymbol{\nabla}\phi_0 = \mathbf{0}. \tag{33}$$

In the following, perturbations of the Cauchy stress tensor $\boldsymbol{\sigma}$ are expressed in terms of the material increment

$$\boldsymbol{\sigma}(\boldsymbol{r}, t) = -p_0(\boldsymbol{x})\,\mathbf{1} + \boldsymbol{\sigma}^\delta(\boldsymbol{x}, t), \tag{34}$$

where the constitutive equations of elastic and viscoelastic materials hold and are expressed as functions of strain and strain rate. The natural choice for perturbations of the total potential ϕ and the of density of the Earth ρ are the local increments

$$\phi(\boldsymbol{r}, t) = \phi_0(\boldsymbol{r}) + \phi^\Delta(\boldsymbol{r}, t), \tag{35}$$

$$\rho(\boldsymbol{r}, t) = \rho_0(\boldsymbol{r}) + \rho^\Delta(\boldsymbol{r}, t). \tag{36}$$

Then, in view of eqs. (31) and (33) and after substitution of eqs. (20) and (34)–(36) into eqs. (19) and (26), we obtain the incremental momentum and Poisson equations

$$\boldsymbol{\nabla}\cdot\boldsymbol{\sigma}^\delta + \boldsymbol{\nabla}\left(\boldsymbol{u}\cdot\boldsymbol{\nabla} p_0\right) - \rho^\Delta\,\boldsymbol{\nabla}\phi_0 - \rho_0\,\boldsymbol{\nabla}\phi^\Delta - \rho^L\,\boldsymbol{\nabla}\phi_0 + \mathbf{M} = \mathbf{0}, \tag{37}$$

$$\nabla^2\phi^\Delta = 4\,\pi\,G\,\left(\rho^\Delta + \rho^L + \rho^T\right) - 2\,\omega^2, \tag{38}$$

where only first-order terms enter. The first term in eq. (37) describes the contribution from the material incremental stress and the second term accounts for the advection of the initial hydrostatic pressure

$$p_0(\boldsymbol{r}) = p_0(\boldsymbol{x}) + \boldsymbol{u}(\boldsymbol{x}, t) \cdot \boldsymbol{\nabla} p_0(\boldsymbol{x}) \tag{39}$$

when eq. (33) is applied at $\boldsymbol{r}$

$$-\boldsymbol{\nabla} p_0(\boldsymbol{r}) - \rho_0(\boldsymbol{r})\, \boldsymbol{\nabla} \phi_0(\boldsymbol{r}) = \boldsymbol{0}. \tag{40}$$

The third term describes the buoyancy forces due to density changes, or compressibility, the fourth term describes the gravity perturbations, or self-gravitation, due to any kind of forcing, and the fifth and sixth terms account for the weight of loads and non-conservative forces: it is clear that the third and fourth terms play a major role in this study devoted to the effects of earthquakes on the gravity field and on compression or dilatation of the Earth's material.

For self-gravitating Earth models, the local incremental potential ϕ^{Δ} must be obtained self-consistently together with the local incremental density ρ^{Δ}. This is accomplished by the coupling of the momentum and Poisson equations, eqs. (37), (38), via the continuity equation of mass written as

$$\rho^{\Delta} = -\boldsymbol{\nabla} \cdot (\rho_0\, \boldsymbol{u}) = -\rho_0\, \Delta - \boldsymbol{u} \cdot \boldsymbol{\nabla} \rho_0. \tag{41}$$

The first term on the RHS describes the density perturbation due to the volume variation Δ of the particle

$$\Delta = \boldsymbol{\nabla} \cdot \boldsymbol{u} \tag{42}$$

and the second term describes the advection of the initial density field. In this respect, the first term on the RHS of eq. (41) is the material incremental density ρ^{δ}

$$\rho^{\delta} = -\rho_0\, \Delta. \tag{43}$$

2˙3. *Compressible and incompressible Earth's models.* – By definition, there are no volume changes Δ within incompressible materials. They occur instead within compressible materials, responsible for differences both in the style of deformation and in the interpretation of density stratifications at the initial state of hydrostatic equilibrium.

During the deformation, incompressible materials react to isotropic stresses. From eq. (4), we require for incompressible materials that the bulk modulus κ is infinitely large in order that the incremental pressure p^{δ} remains finite in the limit of Δ going to zero and of κ going to infinity

$$p^{\delta} = \lim_{\Delta \to 0\, \kappa \to \infty} (-\kappa\, \Delta)\,. \tag{44}$$

In this respect, the bulk modulus is sometimes called modulus of incompressibility. On the contrary, compressible materials are characterized by a finite bulk modulus.

Incompressible and compressible Earth models also differ in their initial state of hydrostatic equilibrium, once the compression of the Earth due to its own weight, or self-compression, is included self-consistently. To better understand this issue, let us consider

the initial density $\rho_0 = \rho(p_0, s_0, c_0)$ as a function of the initial pressure p_0, entropy s_0 and chemical composition c_0 and take its gradient

$$\boldsymbol{\nabla}\rho_0 = \left.\frac{\partial\rho_0}{\partial p}\right|_{s_0,c_0} \boldsymbol{\nabla}p_0 + \left.\frac{\partial\rho_0}{\partial s}\right|_{p_0,c_0} \boldsymbol{\nabla}s_0 + \left.\frac{\partial\rho_0}{\partial c}\right|_{p_0,s_0} \boldsymbol{\nabla}c_0. \tag{45}$$

Let us also assume that the Earth model is spherically symmetric, an assumption that we adopt in our modelling. The initial density, entropy and chemical composition depend only on the radial distance from the Earth centre r leading to

$$\boldsymbol{\nabla}\rho_0 = \partial_r\rho_0\,\boldsymbol{e}_r, \qquad \boldsymbol{\nabla}s_0 = \partial_r s_0\,\boldsymbol{e}_r, \qquad \boldsymbol{\nabla}c_0 = \partial_r c_0\,\boldsymbol{e}_r \tag{46}$$

and, from the condition of hydrostatic equilibrium, eq. (33), the gradient of the initial pressure yields

$$\boldsymbol{\nabla}p_0 = -\rho_0\,\boldsymbol{\nabla}\phi_0 = -\rho_0\,g\,\boldsymbol{e}_r, \tag{47}$$

where $\mathbf{e}_r$ and g are the unit vector pointing outward the Earth's centre and the gravity acceleration for a spherically symmetric Earth

$$g(r) = \frac{4\,\pi\,G}{r^2}\int_0^r \rho_0(r')\,r'^2\,\mathrm{d}r'. \tag{48}$$

Equation (45) can be arranged as follows:

$$\partial_r\rho_0 = -\frac{\rho_0^2\,g}{\kappa} + \gamma, \tag{49}$$

where γ is the compositional coefficient given by

$$\gamma = \left.\frac{\partial\rho}{\partial s}\right|_{p_0,c_0} \partial_r s_0 + \left.\frac{\partial\rho}{\partial c}\right|_{p_0,s_0} \partial_r c_0. \tag{50}$$

Equation (49) is named the generalized Williamson-Adams equation [4, 5]. The first term on the RHS shows how compressibility, via the bulk modulus κ, defines the initial density profile of the Earth. A finite bulk modulus yields a negative density gradient $\partial_r\rho_0$ and the initial density increases with depth according to the compression of the Earth due to its own weight, or self-compression. The second term, the compositional coefficient γ, takes into account the departure from the self-compression due to non-adiabatic and chemically heterogeneous stratifications, when the gradient of the initial entropy, $\partial_r s_0$, and chemical composition, $\partial_r c_0$, differ from zero. Their contribution is at most 10–20 per cent of the actual density gradient of the Earth [6, 5] and it likely occurs in the outermost layers of the Earth, like the transition zone and the lithosphere. The core and the lower mantle, instead, deviate marginally from the adiabatic and chemically homogeneous stratification.

If the stratification is adiabatic and chemically homogeneous we have $\gamma = 0$, which means that the stratification is compressional or in a neutral state of equilibrium. If the stratification is non-adiabatic and chemically heterogeneous we have $\gamma \neq 0$ and is named compositional stratification.

2˙4. *Expansion in spherical harmonics.* – We consider spherically symmetric Earth's models composed of several concentric layers as the core, the lower and upper mantle and the lithosphere. Within each layer the material parameters, consisting of the initial density ρ_0, of the bulk modulus κ, of the shear modulus μ and of the viscosity ν, are continuous functions of only the radial distance from the Earth's centre r. At the internal boundaries separating two layers, these parameters may have step-like discontinuities due to the specific chemical compositions and phases of the rock of each layer.

The most widely used spherically symmetric Earth's model is the Preliminary Reference Earth Model (PREM) [7] that specifies the material parameters of the main layers of the Earth in terms of polynomials of the radial distance from the Earth's centre r. It thus accounts for the continuous variations of the material parameters and for the discontinuities at the interfaces between the layers. Concerning the rheology, we will consider models with a fluid core, a viscoelastic mantle and an elastic lithosphere of about 50 km, in order to evaluate the contribution arising from post-seismic deformation to the gravity anomaly caused by a $M_w = 7$ scenario normal faulting earthquake.

The spherical symmetry of the Earth's model allows to simplify the incremental momentum and Poisson equations and to discuss fundamental aspects of the style of deformation. We thus consider the spherical reference frame and we denote with r, θ and φ the radial distance from the Earth's centre, the colatitude and the longitude, and with $\boldsymbol{e}_r$, $\boldsymbol{e}_\theta$ and $\boldsymbol{e}_\varphi$ the respective unit vectors. Due to the spherical symmetry, the homogeneous differential equations in spheroidal coordinates depend only on the harmonic degree ℓ and not on the order m, once expanded in spherical harmonics: the dependence on the order m is a consequence of the forcing terms representing the body force equivalents to the dislocation or of the asymmetry of the surface or internal load geographical distribution.

Since the spherical harmonics are eigenfunctions of the angular part of the Laplacian operator in spherical coordinates, it is useful to recall herein the expression of the Laplacian operator in spherical coordinates

$$\nabla^2 = \frac{\partial^2}{\partial r^2} + \frac{2}{r}\frac{\partial}{\partial r} + \frac{1}{r^2}\left(\frac{\partial^2}{\partial \theta^2} + \cot\theta\,\frac{\partial}{\partial \theta} + \frac{1}{\sin^2\theta}\frac{\partial^2}{\partial \phi^2}\right). \tag{51}$$

In view of the spherical symmetry, the initial density, potential and pressure depend only on the radial distance from the Earth's centre r and their gradients have no angular components, as already shown in eqs. (46), (47). The incremental momentum and Poisson equations (37), (38) become

$$\boldsymbol{\nabla}\cdot\boldsymbol{\sigma}^\delta - \rho_0\,\boldsymbol{\nabla}\left(g\,\boldsymbol{u}\cdot\boldsymbol{e}_r\right) + \rho_0\,\Delta\,g\,\boldsymbol{e}_r - \rho_0\,\boldsymbol{\nabla}\phi^\Delta - \rho^L\,g\,\boldsymbol{e}_r + \mathbf{M} = \mathbf{0}, \tag{52}$$

$$\nabla^2\phi^\Delta = -4\,\pi\,G\,\left(\rho_0\,\Delta + \partial_r\rho_0\,\boldsymbol{u}\cdot\boldsymbol{e}_r\right) + 4\,\pi\,G\,\left(\rho^L + \rho^T\right) - 2\,\omega^2. \tag{53}$$

We also introduce the spherical harmonic expansions of the potential ϕ and the decomposition of the displacement $\boldsymbol{u}$ into spheroidal, $\boldsymbol{u}_S$, and toroidal, $\boldsymbol{u}_T$, displacements

$$\phi^\Delta(r,\theta,\varphi) = \sum_{\ell=0}^{\infty}\sum_{m=-\ell}^{\ell}\Phi_{\ell m}(r)\,Y_{\ell m}(\theta,\varphi), \tag{54}$$

$$\boldsymbol{u} = \boldsymbol{u}_S + \boldsymbol{u}_T, \tag{55}$$

with

$$\boldsymbol{u}^S(\boldsymbol{r}) = \sum_{\ell=0}^{\infty} \sum_{m=-\ell}^{\ell} \left[U_{\ell m}(r)\, \boldsymbol{R}_{\ell m}(\theta,\phi) + V_{\ell m}(r)\, \boldsymbol{S}_{\ell m}(\theta,\phi) \right], \tag{56}$$

$$\boldsymbol{u}^T(\boldsymbol{r}) = \sum_{\ell=0}^{\infty} \sum_{m=-\ell}^{\ell} W_{\ell m}(r)\, \boldsymbol{T}_{\ell m}(\theta,\phi), \tag{57}$$

$Y_{\ell m}$ denote the spherical harmonics of degree $\ell = 0, \cdots, \infty$ and order $m = -\ell, \cdots, \ell$, and $\boldsymbol{R}_{\ell m}$, $\boldsymbol{S}_{\ell m}$ and $\boldsymbol{T}_{\ell m}$ are the spherical harmonic vectors defined by

$$\boldsymbol{R}_{\ell m} = Y_{\ell m}\, \boldsymbol{e}_r, \tag{58}$$

$$\boldsymbol{S}_{\ell m} = r\, \boldsymbol{\nabla} Y_{\ell m} = \partial_\theta Y_{\ell m}\, \boldsymbol{e}_\theta + \frac{\partial_\varphi Y_{\ell m}}{\sin\theta}\, \boldsymbol{e}_\varphi, \tag{59}$$

$$\boldsymbol{T}_{\ell m} = \boldsymbol{\nabla} \times (\boldsymbol{r}\, Y_{\ell m}) = \frac{\partial_\varphi Y_{\ell m}}{\sin\theta}\, \boldsymbol{e}_\theta - \partial_\theta Y_{\ell m}\, \boldsymbol{e}_\varphi, \tag{60}$$

where $\boldsymbol{r} = r\, \boldsymbol{e}_r$ is the position vector. The scalars $\Phi_{\ell m}$, $U_{\ell m}$, $V_{\ell m}$ and $W_{\ell m}$ are the spherical harmonic coefficients and we refer to them as the potential, the radial and tangential spheroidal displacements, and the toroidal displacement. Note that the spherical harmonic vectors $\boldsymbol{S}_{00}$ and $\boldsymbol{T}_{00}$ yield zero, indicating that the tangential spheroidal and toroidal displacements of harmonic degree $\ell = 0$ do not contribute to deformations. We then set the respective spherical harmonic coefficients to zero, $V_{00} = W_{00} = 0$.

These equations show that the spheroidal and toroidal fields are decoupled and can thus be studied separately. Further details about spherical harmonics and spherical harmonics vectors are discussed in [8]. Here we only explicit the definition of spherical harmonics

$$Y_{\ell m}(\theta,\varphi) = P_{\ell m}(\cos\theta)\, e^{i\, m\, \varphi}, \tag{61}$$

where $P_{\ell m}$ are the associated Legendre polynomials. The latter, for $m \geq 0$, are given by

$$P_{\ell m}(x) = \frac{1}{2^\ell\, \ell!} \left(1 - x^2\right)^{m/2} \frac{d^{\ell+m}(x^2-1)^\ell}{dx^{\ell+m}} \tag{62}$$

and, for $m < 0$,

$$P_{\ell -m}(x) = (-1)^m \frac{(\ell - m)!}{(\ell + m)!}\, P_{\ell m}(x). \tag{63}$$

The spherical harmonics are eigenfunctions of the angular part of the Laplacian operator in spherical coordinates, eq. (51), so that

$$\nabla^2 Y_{\ell m} = \frac{1}{r^2} \left(\frac{\partial^2}{\partial\theta^2} + \cot\theta\, \frac{\partial}{\partial\theta} + \frac{1}{\sin^2\theta} \frac{\partial^2}{\partial\phi^2} \right) Y_{\ell m} = -\frac{\ell(\ell+1)}{r^2}\, Y_{\ell m}. \tag{64}$$

Spherical harmonics are normalized in this work according to

$$\int_\Omega Y_{\ell m} Y^*_{\ell' m'} \mathrm{d}\Omega = N_{\ell m} \delta_{\ell \ell'} \delta_{m m'}, \tag{65}$$

where $N_{\ell m}$ denotes the normalization factor,

$$N_{\ell m} = \frac{4\,\pi}{2\,\ell + 1}\,\frac{(\ell + m)!}{(\ell - m)!}\,, \tag{66}$$

which is the same normalization scheme adopted in [2].

2˙5. *Volume changes and surface forces*. – After substitution of eqs. (55)–(57) into (42), we obtain the spherical harmonic expansion of the volume change Δ

$$\Delta = \boldsymbol{\nabla}\cdot\boldsymbol{u} = \sum_{\ell=0}^{\infty}\sum_{m=-\ell}^{\ell}\chi_{\ell m}\,Y_{\ell m}, \tag{67}$$

where the scalar $\chi_{\ell m}$ is given by

$$\chi_{\ell m} = \partial_r U_{\ell m} + \frac{2}{r}\,U_{\ell m} - \frac{\ell\,(\ell+1)}{r}\,V_{\ell m}. \tag{68}$$

It is noteworthy that the toroidal displacement does not contribute to volume changes, *i.e.*, $\boldsymbol{\nabla}\cdot\boldsymbol{u}_T = 0$. Furthermore, because the toroidal displacement has no component along $\boldsymbol{e}_r$, it does not contribute to the advection of the initial density field of the Earth's models, which can be only radial, as shown by eq. (46). This means that the local incremental density is only due to spheroidal deformations

$$\rho^{\Delta} = -\rho_0\,\boldsymbol{\nabla}\cdot\boldsymbol{u}_S - \partial_r\rho_0\,\boldsymbol{u}_S\cdot\boldsymbol{e}_r \tag{69}$$

and that toroidal deformations do not directly contribute to the local incremental gravitational potential ϕ^{Δ}.

Let us now consider the spherical harmonic expansion of the material incremental stress $\boldsymbol{\sigma}^{\delta}\cdot\boldsymbol{e}_r$ acting on a surface element with outward normal $\boldsymbol{e}_r$. From the definition of the strain tensor and from Hooke's law, eq. (18) or, equivalently, the consitutive equation for the Maxwell solid in the Laplace domain, eq. (16), after some straightforward algebra we obtain

$$\boldsymbol{\sigma}^{\delta}\cdot\boldsymbol{e}_r = \lambda\,\Delta\,\boldsymbol{e}_r + \mu\,\left[\boldsymbol{\nabla}\,(\boldsymbol{u}\cdot\boldsymbol{e}_r) - (\boldsymbol{\nabla}\boldsymbol{e}_r)\cdot\boldsymbol{u} + (\boldsymbol{e}_r\cdot\boldsymbol{\nabla})\,\boldsymbol{u}\right], \tag{70}$$

where λ is the second Lamé parameter that is expressed in terms of the shear modulus μ (also known as first Lamé parameter) and the bulk modulus κ

$$\lambda = \kappa - \frac{2}{3}\,\mu. \tag{71}$$

By substituting the spherical harmonic expansions for displacements and volume changes, eqs. (55)–(57) and (67), we obtain

$$\boldsymbol{\sigma}^{\delta}\cdot\boldsymbol{e}_r = \sum_{\ell m}\left(R_{\ell m}\,\mathbf{R}_{\ell m} + S_{\ell m}\,\mathbf{S}_{\ell m} + T_{\ell m}\,\mathbf{T}_{\ell m}\right), \tag{72}$$

where the spherical harmonic coefficients $R_{\ell m}$, $S_{\ell m}$ and $T_{\ell m}$ are given by

$$R_{\ell m} = \lambda\, \chi_{\ell m} + 2\,\mu\, \partial_r U_{\ell m}, \tag{73}$$

$$S_{\ell m} = \mu \left(\partial_r V_{\ell m} + \frac{U_{\ell m} - V_{\ell m}}{r} \right), \tag{74}$$

$$T_{\ell m} = \mu \left(\partial_r W_{\ell m} - \frac{W_{\ell m}}{r} \right). \tag{75}$$

We will refer to $R_{\ell m}$ and $S_{\ell m}$ as the radial and tangential spheroidal stresses and to $T_{\ell m}$ as the toroidal stress.

2˙6. *Spheroidal deformations.* – The radial and tangential spheroidal components of the momentum equation and the Poisson equation constitute a system of three differential equation of the second order in the unknowns $U_{\ell m}$, $V_{\ell m}$ and $\Phi_{\ell m}$. This differential system must be solved for each harmonic degree from the centre to the surface of the Earth where proper boundary conditions uniquely determine the solution. The treatment of the $\ell = 0$ $\ell = 1$ harmonic components necessitates a peculiar treatment, of no interest in the present work, being the modelling of the gravity anomalies from earthquakes detectable from space gravity missions independent of these $\ell = 0$ $\ell = 1$ components. Analytical solutions of these differential equations can be obtained when the Earth's material is incompressible. In order to take into account the most realistic Earth's material parameters, which require solutions based on numerical techniques for solving the viscoelastic problem for general spherically symmetric Earth's models, we cast these differential equations into the form of six differential equations of the first order that are suitable for numerical integration in the radial variable r by means of algorithms like the Runge-Kutta method. We therefore introduce the spheroidal 6-vector solution $\boldsymbol{y}_{\ell m}$

$$\boldsymbol{y}_{\ell m} = (U_{\ell m},\, V_{\ell m},\, R_{\ell m},\, S_{\ell m},\, \Phi_{\ell m},\, Q_{\ell m})^T\,, \tag{76}$$

where the first and second components are the radial and tangential displacements, the third and fourth components the radial and tangential stresses, the fifth component the potential and the sixth component the so-called "potential stress". The latter is defined as

$$Q_{\ell m} = \partial_r \Phi_{\ell m} + \frac{\ell + 1}{r}\, \Phi_{\ell m} + 4\,\pi\, G\, \rho_0\, U_{\ell m}. \tag{77}$$

From the radial and tangential spheroidal components of the momentum equation, from the Poisson equation and the definition of radial, tangential and potential stresses, eqs. (73)-(74) and (77), after some algebra we obtain the following linear differential system for the spheroidal vector solution:

$$\frac{\mathrm{d}\boldsymbol{y}_{\ell m}(r)}{\mathrm{d}r} = \mathbf{A}_\ell(r)\, \boldsymbol{y}_{\ell m}(r) - \boldsymbol{f}_{\ell m}(r), \tag{78}$$

where $\mathbf{A}_\ell$ is the 6×6-matrix depending on the material parameters of the Earth's model,

on the radial distance from the Earth centre r and on the harmonic degree ℓ

$$\mathbf{A}_\ell(r) = \tag{79}$$

$$\begin{pmatrix} -\frac{2\,\lambda}{r\,\beta} & \frac{\ell(\ell+1)\,\lambda}{r\,\beta} & \frac{1}{\beta} & 0 & 0 & 0 \\ -\frac{1}{r} & \frac{1}{r} & 0 & \frac{1}{\mu} & 0 & 0 \\ \frac{4}{r}\left(\frac{3\,\kappa\,\mu}{r\,\beta} - \rho_0\,g\right) & \frac{\ell(\ell+1)}{r}\left(\rho_0\,g - \frac{6\,\kappa\,\mu}{r\,\beta}\right) & -\frac{4\,\mu}{r\,\beta} & \frac{\ell(\ell+1)}{r} & -\frac{\rho_0(\ell+1)}{r} & \rho_0 \\ \frac{1}{r}\left(\rho_0\,g - \frac{6\,\mu\,\kappa}{r\,\beta}\right) & \frac{2\,\mu}{r^2}\left[\ell(\ell+1)\left(1+\frac{\lambda}{\beta}\right) - 1\right] & -\frac{\lambda}{r\,\beta} & -\frac{3}{r} & \frac{\rho_0}{r} & 0 \\ -4\,\pi\,G\,\rho_0 & 0 & 0 & 0 & -\frac{\ell+1}{r} & 1 \\ -\frac{4\,\pi\,G\,\rho_0\,(\ell+1)}{r} & \frac{4\,\pi\,G\,\rho_0\,\ell(\ell+1)}{r} & 0 & 0 & 0 & \frac{\ell-1}{r} \end{pmatrix},$$

with

$$\beta = \lambda + 2\,\mu. \tag{80}$$

The non-homogeneous term $\boldsymbol{f}_{\ell m}$ of the differential system (78) accounts for terms related to massive bodies other than the Earth and for seismic forces, responsible for the ℓ, m dependence. In fact, the homogeneous system depends solely on the harmonic degree ℓ being the Earth's model spherically symmetric, while the seismic equivalent body forces are intrinsically non-symmetric, or dependent also on the order m, similar to surface or internal loads which can introduce the m dependence through their geographical distribution along longitude. The explicit expression of the $\boldsymbol{f}_{\ell m}(r)$ term is given in sect. 1.10 "Point Sources" of ref. [2], for internal loads and seismic sources.

Similarly to the case of spheroidal deformations, we define the toroidal 2-vector solution $\boldsymbol{y}_{\ell m}$ as follows:

$$\boldsymbol{y}_{\ell m} = (W_{\ell m},\, T_{\ell m})^T\,, \tag{81}$$

where the first and second components are the toroidal displacement and stress, respectively. The toroidal component of the momentum equation can be cast into a linear differential system like eq. (78)

$$\frac{\mathrm{d}\boldsymbol{y}_{\ell m}(r)}{\mathrm{d}r} = \mathbf{A}_\ell(r)\,\boldsymbol{y}_{\ell m}(r) - \boldsymbol{f}_{\ell m}(r), \tag{82}$$

where now $\boldsymbol{y}_{\ell m}$ and $\mathbf{A}_\ell$ are the toroidal 2-vector solution (81) and the following 2×2-matrix:

$$\mathbf{A}_\ell = \begin{pmatrix} \dfrac{1}{r} & \dfrac{1}{\mu} \\ \dfrac{\mu(\ell(\ell+1)-2)}{r^2} & -\dfrac{3}{r} \end{pmatrix} \tag{83}$$

and the dishomogeneous term $\mathbf{f}_{\ell m}$ accounts for the toroidal components of the seismic forces.

The explicit expression of the seismic forcing, relevant for studying the earthquake effects on the gravity field, can be found in sect. 1.10.2 "Fault discontinuities" of [2], based on the work of [9, 8], which introduce the m dependence in the solutions of the spheroidal and toroidal systems of differential equations. From now on, we consider only the spheroidal part of the solution, since the we are interested in the gravitational effects of the earthquakes, which depend only on the spheroidal part, since the toroidal part does not affect the gravity.

2˙7. *Elastic and viscoelastic solutions.* – The general solution of the differential system (78) or (82) reads

$$\mathbf{y}_{\ell m}(r) = \mathbf{\Pi}_\ell(r, r_0)\mathbf{y}_0 - \int_{r_0}^{r} \mathbf{\Pi}_\ell(r, r')\, \boldsymbol{f}_{\ell m}(r')\, \mathrm{d}r', \tag{84}$$

where $\mathbf{y}_0$ is the Cauchy datum at the radius r_0

$$\mathbf{y}_{\ell m}(r_0) = \mathbf{y}_0 \tag{85}$$

and $\mathbf{\Pi}_\ell$ is the so-called propagator matrix. The latter is the 6×6-matrix for the spheroidal case and the 2×2-matrix for the toroidal case that solve the following homogeneous differential system:

$$\frac{\mathrm{d}\mathbf{\Pi}_\ell(r, r')}{\mathrm{d}r} = \mathbf{A}_\ell(r)\, \mathbf{\Pi}_\ell(r, r'), \tag{86}$$

with the Cauchy datum at the radius r' given by the identity matrix $\mathbf{1}$

$$\mathbf{\Pi}_\ell(r', r') = \mathbf{1}. \tag{87}$$

For the toroidal case, the forcing term is limited to the seismic sources. In this respect, each column of the propagator matrix is one of the six linearly independent solutions of the homogeneous differential system

$$\frac{\mathrm{d}\mathbf{y}_{\ell m}}{\mathrm{d}r} = \mathbf{A}_\ell\, \mathbf{y}_{\ell m}. \tag{88}$$

When the integration of eq. (86) in a viscoelastic layer of the Earth's model arrives at an internal chemical boundary, we impose the continuity of the propagator and we continue the integration in the new layer according to the continuity of the spheroidal and toroidal solution vectors at each chemical interface

$$\mathbf{\Pi}_\ell(r_j^+, r') = \mathbf{\Pi}_\ell(r_j^-, r'). \tag{89}$$

In this way the spheroidal and toroidal vector solutions $\boldsymbol{y}_{\ell m}$, eq. (84), satisfy the conditions for the chemical boundaries between the viscoelastic layers of the Earth's model.

We impose CMB (Core Mantle Boundary) conditions in the general solution (84) by choosing the bottom of the mantle as the radius from which the integration starts, $r_0 = r_C^+$, and equating the Cauchy datum $\mathbf{y}_0$ as follows:

$$\mathbf{y}_{\ell m}(r_C^+) = \mathbf{y}_0 = \mathbf{I}_C\, \mathbf{C}, \tag{90}$$

where $\mathbf{y}_0 = \mathbf{I}_C\,\mathbf{C}$, with the $\mathbf{C}$ vector denoting the three integration constants, is the solution vector at the outer boundary of the Earth's core, which is assumed to be an inviscid fluid, which is appropriate for short-time events like earthquakes as indicated by the shear waves which do not cross the outer core. The complete treatment of the CMB conditions can be found in sect. 1.6.3 "Core-mantle boundary" in [2].

This yields

$$\mathbf{y}_{\ell m}(r) = \mathbf{\Pi}_\ell(r, r_C^+)\mathbf{I}_C\mathbf{C} - \mathbf{w}(r), \tag{91}$$

where, for brevity, we have defined

$$\mathbf{w}(r) = \int_{r_C^+}^{r} \mathbf{\Pi}_\ell(r, r')\, \boldsymbol{f}_{\ell m}(r')\, \mathrm{d}r', \tag{92}$$

without the explicit dependence on ℓ, m to not overwhelm the following equations.

The three constants of integration $\mathbf{C}$ entering the CMB conditions are estimated by imposing the boundary conditions at the Earth's surface related to the radial and tangential stress and to the gravitational potential stress. From eq. (91) and by recalling that the spheroidal vector solution refers to the solution just below the Earth's surface, we write

$$\mathbf{P}_1\mathbf{y}_{\ell m}(a^-) = \mathbf{P}_1\left(\mathbf{\Pi}_\ell(a^-, r_C^+)\mathbf{I}_C\mathbf{C} - \mathbf{w}(a^-)\right) = \boldsymbol{b}, \tag{93}$$

where $\mathbf{P}_1$ denotes a projection matrix picking the radial and tangential components of the stress and the gravitational potential stress from the solution vector, to match at the Earth's surface the corresponding values of these quantities provided by the $\boldsymbol{b}$ vector, which is zero for the toroidal part. The $\boldsymbol{b}$ vector accounts for the boundary conditions at the Earth's surface, such as surface density anomalies, tidal and centrifugal potentials and is explicitly given in sect. 1.6.1 "The Earth's surface" in [2] in terms of the spherical harmonic components of these forcings.

Note that $\mathbf{w}$ is evaluated at a^-, which means that the integration from the bottom of the mantle entering eq. (92) ends just below the Earth's surface, a^-. This means that surface loadings do not contribute to the integral since their effect is already accounted for by the Earth's surface boundary condition via the $\boldsymbol{b}$ term. In other words, the vector solution must be intended as evaluated below the Earth surface a because it refers to perturbations of the Earth, and only the density of internal loads and seismic forces contribute to the vector $\mathbf{w}$. The dishomogeneous term $\boldsymbol{f}_{\ell m}$ does not thus include those terms that are zero within the Earth, *i.e.*, the surface density $\sigma_{\ell m}^L$ and the density of external bodies $\rho_{\ell m}^T$

$$\boldsymbol{f}_{\ell m} = \rho_{\ell m}^I\, \boldsymbol{f}^L + \boldsymbol{m}_{\ell m}, \tag{94}$$

where the superscript I for internal loads is used rather than the more general L; the toroidal case is limited to the solely seismic term denoted by the second term on the RHS.

Then, using eq. (93) for obtaining the constants of integration $\mathbf{C}$

$$\mathbf{C} = \left(\mathbf{P}_1\, \mathbf{\Pi}_\ell(a, r_C)\, \mathbf{I}_C\right)^{-1}\, \left(\mathbf{P}_1\, \mathbf{w}(a) + \boldsymbol{b}\right) \tag{95}$$

where now the minus sign is omitted in a^- and the plus sign is omitted in r_C^+, eq. (91) becomes

$$\mathbf{y}_{\ell m}(r) = \mathbf{\Pi}_\ell(r, r_C)\mathbf{I}_C \, (\mathbf{P}_1 \, \mathbf{\Pi}_\ell(a, r_C) \, \mathbf{I}_C)^{-1} \, (\mathbf{P}_1 \, \mathbf{w}(a) + \boldsymbol{b}) - \mathbf{w}(r). \tag{96}$$

This is the solution of the associated elastic problem that uniquely determines the spheroidal deformations and the perturbations of the potential within the Earth, as well as the radial and tangential spheroidal stresses and the potential stress, in response to internal and surface loading, and tidal, centrifugal and seismic forcings. It is notable that, although the propagator or the solution of the homogeneous differential equation system depends solely on the harmonic degree ℓ, the non-homogeneous forcing term, in our case associated to the seismic forcing, depends also on the order m: it is clear that in order to "see" in the gravity field the gravity signal from earthquakes, we need a gravity probe which has the capability to scan from space the whole Earth along latitude and longitude. In the following sect. **4** we show that we have nowadays at disposal such a breakthrough instrumentation, to be mounted on board of the incoming NGGM missions.

3. – The relaxation spectrum

Within the perspective of applications of the present theory to the modeling of geodetic observations, we consider the solution, denoted by $\mathbf{K}$, for the radial and tangential spheroidal displacements and local incremental potential at the Earth's surface

$$\mathbf{K}_{\ell m}(a) = \begin{pmatrix} U_{\ell m}(a) \\ V_{\ell m}(a) \\ \Phi_{\ell m}(a) \end{pmatrix}. \tag{97}$$

From eq. (96) we obtain

$$\mathbf{K}_{\ell m}(a) = \mathbf{P}_2 \, \mathbf{y}_{\ell m}(a) = \mathbf{B}_\ell(a) \, (\mathbf{P}_1 \, \mathbf{w}(a) + \boldsymbol{b}) - \mathbf{P}_2 \, \mathbf{w}(a), \tag{98}$$

where $\mathbf{P}_2$ is the projector for the first, second and fifth components of the spheroidal vector solution and, for brevity, we have defined

$$\mathbf{B}_\ell(r) = \mathbf{P}_2 \mathbf{\Pi}_\ell(r, r_C)\mathbf{I}_C \, (\mathbf{P}_1 \, \mathbf{\Pi}_\ell(a, r_C) \, \mathbf{I}_C)^{-1}. \tag{99}$$

When we integrate along the Bromwich contour in order to apply the Correspondence Principle and to obtain the viscoelastic solution by anti-transforming from the Laplace domain to the time domain the $\mathbf{B}_\ell(r)$ matrix, we have to deal with the singularities of the propagator $\mathbf{\Pi}_\ell(r, r_C)$ and of the inverse of the matrix $\mathbf{P}_1 \, \mathbf{\Pi}_\ell(a, r_C) \, \mathbf{I}_C$ arising from different sources, within the complex closed contour in the Laplace domain.

The first source of singularities arises when the differential system (86) is non-uniformly Lipschitzian, not satisfying the Lipschitz condition

$$|f(r) - f(r')| \leq K \, |r - r'|, \quad \forall \, (r, r') \in [r_C, a], \tag{100}$$

where K a positive constant, due to the singularities of the propagator matrix $\mathbf{\Pi}_\ell$: inspection of the function $\hat{\mu}(s)$ and of the elements of the matrix $\mathbf{A}_\ell$, defined in eqs. (17)

and (79), leads to the conclusion that the differential system is not uniformly Lipschitzian for $s = 0$, $s = -\tau^{-1}$ and $s = -\varsigma^{-1}$, where ς is the so-called compressional transient time [10, 4] defined as

$$\varsigma = \tau \left(1 + \frac{4\,\mu}{3\,\kappa}\right), \tag{101}$$

which makes singular some elements of the $\mathbf{A}_\ell$ matrix given by eq. (79), being responsible for $\beta = 0$ in eq. (80) once $\hat{\mu}(s)$, eq. (17), is considered.

We denote the set of non-uniformly Lipschitzian zones as $\mathcal{N}$

$$\mathcal{N} = \{0\} \cup \mathcal{N}_\tau \cup \mathcal{N}_\varsigma, \tag{102}$$

with

$$\mathcal{N}_\tau = \left\{ s \in \mathbb{R} \,\middle|\, s = -\frac{1}{\tau(r)} \;\forall\, r \in [r_C, a] \right\}, \tag{103}$$

$$\mathcal{N}_\varsigma = \left\{ s \in \mathbb{R} \,\middle|\, s = -\frac{1}{\varsigma(r)} \;\forall\, r \in [r_C, a] \right\}. \tag{104}$$

This singularity at the origin of the Laplace domain occurs because $\hat{\mu}(s = 0) = 0$ and the momentum equation becomes the equation for the inviscid body. This demands a specific treatment, like that for the inviscid core. Cambiotti and Sabadini [4] show that the origin of the Laplace domain is not a singularity if the stratification of the mantle is compressional ($\gamma = 0$), while it is the cluster point of a infinite denumerable set of roots if the stratification is compositional ($\gamma \neq 0$).

The second source of singularities comes from the constants of integration $\mathbf{C}$ using the boundary conditions at the Earth's surface, eq. (95). Indeed, the inverse of the 3×3-matrix $[\mathbf{P}_1 \mathbf{\Pi}_\ell(a, r)\, \mathbf{I}_C]_{\mu=\hat{\mu}(s)}$ may be singular for some value of the Laplace variable s. In this respect, we recast the matrix $\mathbf{B}_\ell$ as follows:

$$\mathbf{B}_\ell(r)|_{\mu=\hat{\mu}(s)} = \frac{(\mathbf{P}_2 \mathbf{\Pi}_\ell(r, r_C)\, \mathbf{I}_C)\, (\mathbf{P}_1 \mathbf{\Pi}_\ell(a, r_C)\, \mathbf{I}_C)^\dagger|_{\mu=\hat{\mu}(s)}}{D(s)}, \tag{105}$$

where $\dagger$ stands for the matrix of the complementary minors, and $D(s)$ is the so-called secular determinant

$$D(s) = \det\left(\mathbf{P}_1 \mathbf{\Pi}_\ell(a, r)\, \mathbf{I}_C\right)|_{\mu=\hat{\mu}(s)}. \tag{106}$$

The singularities thus occur for the solutions of the so-called secular equation

$$D(s) = 0, \tag{107}$$

when the secular determinant entering the denominator of eq. (105) is zero. As proved by [11] these solutions must be on the real axis of the Laplace domain, *i.e.*, $\Im s = 0$. We denote the set of these singularities as $\mathcal{S}$

$$\mathcal{S} = \{s \in \mathbb{R} \mid D(s) = 0\}. \tag{108}$$

Experience and analytical proofs have led to the conclusion that the solution s_j of the secular equation (107) are finite or, at most infinite denumerable (they may have cluster points belonging to the non-uniformly Lipschitzian zone $\mathcal{N}$). Furthermore, they are first-order roots and, in this respect, the solution vector in the Laplace domain has first-order poles at these roots. This is the simplest type of singularity we deal with by means of the residue theorem, obtaining $e^{s_j\,t}$ exponentials in the time domain. Particularly, each root s_j contributes to the complex integration along the closed contour Γ for the Green function $\boldsymbol{k}(s)$ entering the definition of the $\mathbf{K}_{\ell m}(a)$ matrix as detailed in [2]

$$\frac{1}{2\pi i}\oint_{\Gamma_j}\boldsymbol{k}(s)\,e^{s\,t}\mathrm{d}s=\boldsymbol{k}_j\,e^{s_j\,t}, \tag{109}$$

where s_j and Γ_j denote the j-th first-order pole and the closed path containing only this root, and $\boldsymbol{k}_j$ is the residue

$$\boldsymbol{k}_j=\lim_{s\to s_j}(s-s_j)\boldsymbol{k}(s) \tag{110}$$

on the basis of the residue theorem.

This shows that each root s_j is associated with a response of the viscoelastic Earth's model due to the imposition of any kind of forcing or external potentials, as the tidal or centrifugal ones. These responses are called normal modes and have characteristic relaxation times t_j given by the inverse of the root s_j. They describe the transition from the elastic to the fluid behaviour due to viscoelastic relaxation of deviatoric stress. The roots s_j depend generally on the material parameters of all the layers of the viscoelastic Earth model and on the harmonic degree ℓ (and thus must be determined for each harmonic degree). The roots s_j are negative but density inversion at the internal interfaces between the layers of the model, when the density of the layers is lower than that of the neighboring layer above [12, 13], and unstable compositional stratifications, for positive compositional coefficients $\gamma > 0$ [10, 4], trigger positive normal mode roots s_j. According to eq. (109), these positive roots are responsible for the divergence of the displacements and of the potential at large time scales, called Rayleigh-Taylor instabilities. If that is the case, unstable convective motions will be triggered in the Earth's model and the theory as developed in [2] breaks down on time scales comparable with the characteristic relaxation time of Rayleigh-Taylor instabilities, $t_j = -/s_j$.

For simple layered incompressible models, the total number of normal modes is finite and can be determined by means of the following rules:

- At each boundary between two viscoelastic layers, one buoyancy mode is triggered if the densities on both sides of the boundary are different. Buoyancy modes between two mantle layers are labelled Mi, with $i = 1, 2, \cdots$. At the same boundary, two additional relaxation modes are triggered if the Maxwell times of both sides of the boundary are different. These paired modes are called transient viscoelastic modes as they have relatively short relaxation times and therefore labelled Ti^+ and Ti^-, with $i = 1, 2, \cdots$.
- If one side of the boundary is elastic and the other is viscoelastic, as the interface between the elastic lithosphere and the viscoelastic mantle, one buoyancy mode and one transient viscoelastic mode are triggered, labelled $M0$ and $L0$ in this case of the lithosphere, the first due to the density contrast between the atmosphere and the viscoelastic mantle beneath the lithosphere.

– If the lithosphere is viscoelastic or we consider the viscoelastic upper mantle as the outermost layer, the viscoelastic Earth's surface contributes with a buoyancy mode that is also labelled $M0$, similarly to the viscoelastic mode $M0$ triggered at the interface between the elastic lithosphere and the viscoelastic mantle.

– The core-mantle boundary contributes with one buoyancy mode, labelled $C0$.

In order to gain insights into the physics of the relaxation processes, it is important to take a close look at the relaxation times corresponding to the modes excited by discontinuities in the physical parameters of simple Earth's models, such as the incompressible one described herein in table I in terms of the density, rigidity and of the depth of the major layers building our planet, and verify that the number of modes matches the rules stated above.

We will consider the spheroidal case, contributing to the perturbation in the gravity from earthquakes or from any other source. Building the propagator and deriving the normalized secular determinant $D(s)$ entering eq. (102), fig. 1 portrays $f(D_\ell(s)) = \mathrm{sgn}(D_\ell(s)) \times \log_{10}(|D_\ell(s)|)$ if $|D(s)| > 10.0$ and $f(D_\ell(s)) = D_\ell(s)/10.0$ if $|D_\ell(s)| \leq 10.0$ as function of $\log_{10}(-1/(s \times \mathrm{kyr}))$, which means that s, negative, expressed in 1/sec is normalized by $1\,\mathrm{kyr} = 3.153 \times 10^{10}\,\mathrm{sec}$, for the harmonic degrees $\ell = 2$, 10 and 100, from top to bottom and for the 5-layer, incompressible Earth's model displayed in table I. The zero crossings are the relaxation times corresponding to the normal modes $T_i = -1/s_i$ of the 5-layer Earth's model. Figure 1 portrays 9 zero crossings, or normal modes of the secular determinant $D(s)$ as expected for the five-layer model of table I: four transient modes $T1$–$T4$ are triggered at the two interfaces between the viscoelastic layers, at 5951 and 5701 km, because their Maxwell times are different (from table I); two buoyancy modes, $M1$ and $M2$ are triggered at these two interfaces between viscoelastic layers, $M1$ at 5701 and $M2$ at 5951 km; the density contrast between the viscoelastic mantle and the atmosphere triggers the mantle mode $M0$, the rheological contrast between the viscoelastic mantle and the elastic lithosphere triggers $L0$ and finally the density contrast between the mantle and the core triggers the core mode $C0$, giving a final total count of nine modes. The slowest modes have been named $M1$ and $M2$ and are associated with the two internal chemical boundaries at 670 and 420 km. These $M1$ and $M2$ modes are important when dealing with the geophysical processes affected by the slow readjustment of internal density discontinuities, as for the post-seismic phase.

The longest T_i correspond to the buoyancy $M2$ and $M1$ modes in the extreme right

TABLE I. – *Parameters for the 5-layer fixed-boundary contrast Earth model. r is the distance with respect to the centre of the Earth, ρ the density of the layer, and μ the rigidity.*

Layer	r (km)	ρ (kg/m^3)	ν (Pa s)	μ (N/m^2)	
1	6371–6251	3070	elastic	5.76×10^{10}	lithosphere
2	6251–5951	3070	10^{21}	5.76×10^{10}	shallow upper mantle
3	5951–5701	3850	10^{21}	1.06×10^{11}	transition zone
4	5701–3480	4970	10^{21}	2.16×10^{11}	lower mantle
5	3480–0	10750	inviscid	0	inviscid fluid core

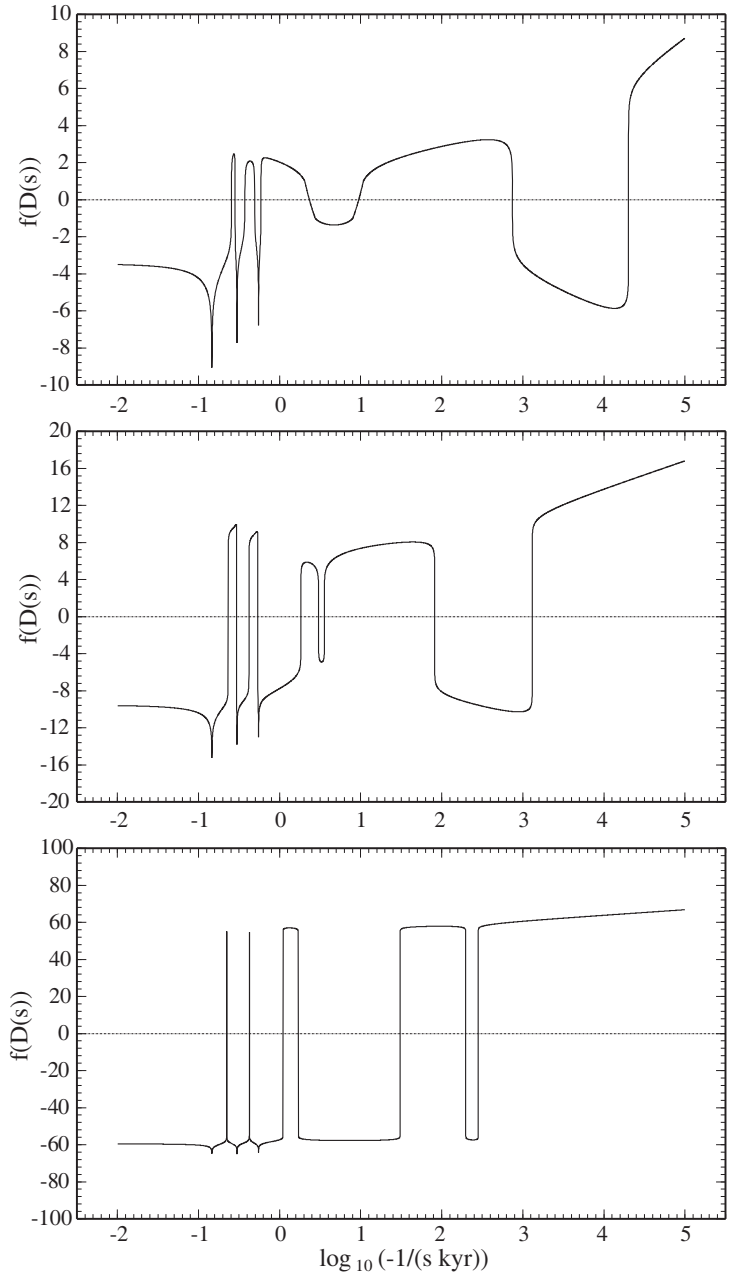

Fig. 1. – With s normalized by 1 kyr, plot of the function defined as $f(D_\ell(s)) = \mathrm{sgn}(D_\ell(s)) \times \log_{10}(|D_\ell(s)|)$ if $|D(s)| > 10.0$ and $f(D_\ell(s)) = D_\ell(s)/10.0$ if $|D_\ell(s)| \leq 10.0$ as a function of $\log_{10}(-1/(s \times \mathrm{kyr}))$ and its zero crossings, providing the relaxation times $T_i = -1/s_i$, for the 5-layer incompressible model of table I and $l = 2, 10, 100$ from top to bottom. This calculation and corresponding figure have been kindly provided by Shuang Yi, from the Key Laboratory of Computational Geodynamics from the University of the Chinese Academy of Sciences (UCAS), January 2015. This figure is fig. 2.2 of [2].

of the abscissa, and for $\ell = 2$ they are $T_{M2} = 2.01 \times 10^7$ yr, $T_{M1} = 7.44 \times 10^5$ yr, due to density contrasts between viscoelastic internal layers. To the left, towards shorter times, we catch the core mode $C0 = 9.48 \times 10^3$ yr, the mantle mode $M0 = 2.33 \times 10^3$ yr, the lithospheric mode $L0 = 5.89 \times 10^2$ yr and then, at the shortest times, the couple of transient relaxation times $T1$–$T4$, 4.92×10^2, 3.73×10^2, 2.83×10^2 and 2.55×10^2 yr. Increasing the harmonic degree at $\ell = 10$ the transient relaxation times remain constant, while the three modes $L0$, $M0$ and $C0$ move to the right, towards longer times, while $M1$ and $M2$ do the opposite. When $\ell = 100$ the transient modes merge together and the two adjacent modes become indistinguishable at this scale, apparently reducing the nine modes to seven modes. The lithospheric mode $L0$ moves towards the slowest $M1$, $M2$ modes, while the latter get close to one another.

Density contrasts thus provide the most important modal contributions, the buoyancy modes, and the amplitude of the former, and the depth where these modes are triggered, determine the characteristic time scale over which the density contrast interface adjusts once displaced by any geophysical forcing. Each mode contribution, due to density, viscosity, elasticity contrasts, or due to compressional dilatation and contraction, as hereinafter, has its own clear and simple physical explanation.

Compressible layered models and the self-compressed compressible sphere share the same normal modes of layered incompressible models and additional relaxations modes associated to compressibility [10, 4]:

– Each viscoelastic compressible layer triggers two modes. These paired modes are called transient compressible modes as they have relatively short relaxation times and usually labelled $\mathrm{Z}i^+$ and $\mathrm{Z}i^-$, with $i = 1, 2, \cdots$. Within the same layer, also an infinite denumerable set of modes is triggered. They are called dilatational modes, labelled D_j, with $j = 1, \cdots, \infty$, and their characteristic times converge to the compressional transient time ς in the limit for $j \to \infty$

$$\lim_{j\to\infty} s_{\mathrm{D}_j} = -\varsigma^{-1}. \tag{111}$$

The normal modes defined above complete those for compressible Earth's models with compressional stratifications ($\gamma = 0$), when the initial density stratification is due to the only self-compression of the Earth. Instead, compositional stratifications ($\gamma \neq 0$) trigger another infinite denumerable set of buoyancy modes with very long characteristic times. They are called compositional modes, labelled C_j, with $j = 1, \cdots, \infty$. These modes can be both stable, $s_{\mathrm{C}_j} < 0$, and unstable, $s_{\mathrm{C}_j} > 0$, and their poles s_{C_j} monotonically converge to the origin of the Laplace domain for $j \to \infty$

$$\lim_{j\to\infty} s_{\mathrm{C}_j} = 0. \tag{112}$$

In the unstable case the compositional modes describe Rayleigh-Taylor instabilities that occur on time scales of the order of the shortest characteristic time $t_{\mathrm{C}_1} = -1/s_{\mathrm{C}_1}$, with $j = 1$.

The presence of dilatational and compositional modes arises theoretical and computational problems in obtaining all the contributions from normal modes, eq. (109). However, it is sufficient to detect the first few of these modes in order that the Green functions converge to the exact ones. In fact, for $j \to \infty$, the residues $\boldsymbol{k}_{\mathrm{D}_j}$ and $\boldsymbol{k}_{\mathrm{C}_j}$ of

dilatational and compositional modes go to zero sufficiently fast so that their summation converges once the first few of them are taken into account [10, 4].

Modal components to the deformation and gravity, resulting from the Correspondence Principle, provide us with a clear physics and make possible a deep comprehension of the intimate nature of the viscoelastic behaviour of the Earth, which would be impossible to attain, for example, via standard integration in time.

It is thus possible, with the above rules, to determine the total number of modes of eq. (107): the possibility of knowing in advance the total number of modes triggered by the Earth's model is quite useful, since this equation must be solved numerically and this root-solving procedure is the only non-analytical part of the viscoelastic relaxation method when incompressible models are considered.

The root-solving procedure usually consists of two parts: grid-spacing, followed by a bisection algorithm. In the grid-spacing part, the s-domain is split into a number of discrete intervals. For each s-value at a boundary of an interval, the value of the determinant expressed by eq. (107) is calculated, after which this value is multiplied by the value of the determinant of the s-value of the boundary next to it. If this product is positive, then the determinant has not changed in sign (or has changed an even number of times). If the product is negative, then we are sure that there is (at least) one root inside the interval bounded by the two s-values for which the determinant was calculated. In that case, the interval is split up in two parts, and the procedure of determining the product of the determinant of the bounding s-values is repeated. The interval where the determinant changes sign will result again in a negative product, and for this interval the procedure of cutting the interval in two, etc., is repeated. Thus the s-value where the determinant is equal to zero as in eq. (107) becomes progressively better estimated with each further step in this bisection algorithm. Of course, it can happen that the determinant changes sign over a small s-interval twice or even more times. It is thus necessary to choose small grids in the s-domain (in practice, it appears that especially the two modes of each T-mode pair have inverse relaxation times (s-values) that are very close to each other). Only after the complete number (determined with the rules above) of roots/modes of eq. (107) has been found can one be sure that the complete signal will be retrieved after inverse-Laplace transformation. For this final step in the relaxation modeling procedure we use the so-called method of complex contour integration.

3˙1. *Modal and non-modal contributions.* – The Green function $\tilde{\boldsymbol{k}}(s)$ has thus two different types of non-analyticity. The first comes from a denumerable set of poles $s_j \in \mathcal{S}_0$. The second comes from the continuous set $\mathcal{N}$ of the Maxwell and compressional transient times τ and ς. According to [14], we will refer to these contributions as the "modal" and "non-modal" contributions. The modal contribution can be explicited in the viscoelastic Green function by making use of the residue theorem as in eq. (109)

$$\boldsymbol{k}_V(t) = \sum_{s_j \in \mathcal{S}_0} \boldsymbol{k}_j \, e^{s_j \, t} + \frac{1}{2\,\pi\,i} \oint_{\Gamma} \boldsymbol{k}_N(s)\,\mathrm{d}s + \boldsymbol{k}_E \, \delta(t), \tag{113}$$

where $\boldsymbol{k}_V(t)$ stands for the viscous part of the Green function and $\tilde{\boldsymbol{k}}_N(s)$ stands for the non-modal contribution that we cannot further explicit and must be obtained by complex integration along the closed contour Γ.

The non-modal contribution is inherently associated with the continuous variations of the Maxwell and compressional transient times. Indeed these singularities do not

contribute to the perturbations in the time domain if they are isolated points in the Laplace s-domain [10, 15, 16]. This is the case for layered Earth's models, where the elastic parameter and the viscosity are constant within each layer, because the Maxwell and compressional transient times do not vary within each layer. Equation (113) thus becomes

$$\boldsymbol{k}_V(t) = \sum_{s_j \in \mathcal{S}_0} \boldsymbol{k}_j \, e^{s_j \, t}. \tag{114}$$

On the contrary, we have verified that a non-zero contribution comes from the set $\mathcal{N}$ when it is continuous [4] and we must evaluate the complex contour integration along the contour Γ in eq. (113).

4. – Next-generation gravity missions

The past generation of satellites devoted to measuring Earth's gravity included GOCE, a project of the European Space Agency in orbit from 2009 to 2013, and GRACE, a collaboration project of NASA and the German Space Agency DLR, launched in 2002 and operating till late 2017. GOCE provided static full tensor gravity gradients over the entire Earth (except 7 deg wide polar caps) with spatial resolution of about 200 km. GRACE measured the time variation of the gravity gradient over a 220 km baseline with about 500 km spatial resolution at 1 month intervals between successive gravity maps. Continuity of the GRACE data series will be ensured by the GRACE Follow-On (GFO) mission, launched in 2018. GFO is built on the GRACE blueprint with partial spacecraft improvements and carries an experimental laser interferometer payload. On a longer perspective, both ESA and NASA are considering next-generation gravity missions (NGGM) aiming to measure the temporal variations of the Earth's gravity field over a time span of several years with spatial resolution around 100 km and time resolution of a few days. Recently, the successor to GRACE and GFO was recommended as a top priority of the US Decadal Strategy for Earth Observation from Space. Low Earth orbit satellite-to-satellite tracking (SST) is the technique for recovering the tiny time-variable gravity field signal [17]. In this approach the gravity sensor consists of a pair of satellites flying in loose formation and the measured quantity is the distance variation between the satellites (d in fig. 2) induced by the gravity anomalies. Accelerometers on each satellite measure the non-gravitational accelerations F_{Di} produced by atmospheric drag, which are separated from the gravity signal in the post-flight data processing. Like GRACE, the NGGM will use the SST technique, but replacing the current radiofrequency ranging system with a laser interferometer. Further improvements will come from flying on a low, constant altitude orbit with the drag disturbances abated by drag-free control, a technique demonstrated in GOCE. Furthermore, the temporal resolution in Earth's gravity sampling can be enhanced by flying two satellite pairs in the so-called Bender constellation [18]: one pair in a near-polar orbit and one pair in a medium-inclination orbit, as shown in fig. 3. The optimization of the satellite constellation for NGGM has been the subject of a dedicated, ESA-funded study [19], which established the achievable performance in the retrieval of the gravity field. This performance is consistent with measuring the gravity anomalies caused by earthquakes with magnitudes lower than the currently achieved $M_w = 8.5$–9. Moreover, two pairs of satellites can provide homogenous coverage of the Earth leading to gravity field solutions with a revisiting frequency of 3 days, allowing to separate the co- and post-seismic contributions. As clearly portrayed

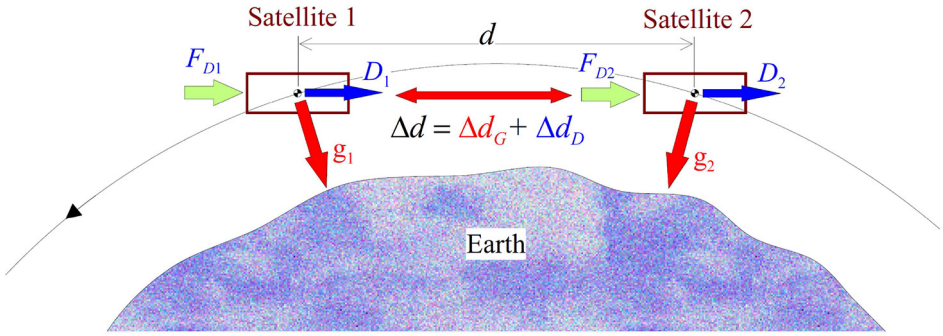

Fig. 2. – SST technique, courtesy of Thales Alenia Space in Italy.

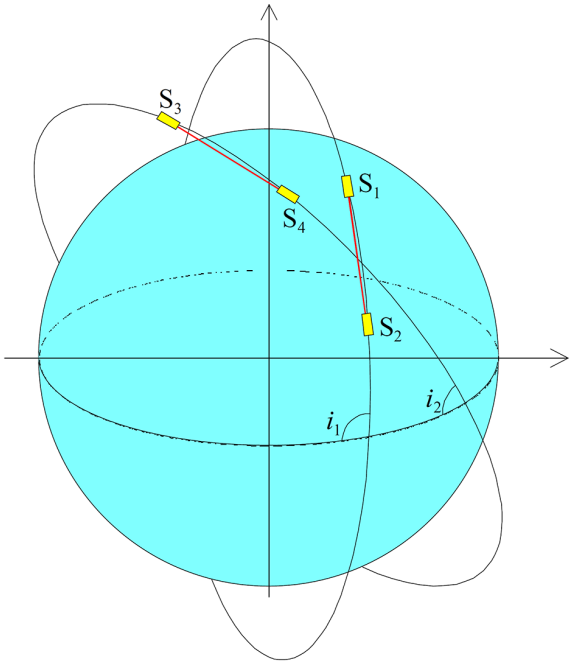

Fig. 3. – Satellite constellation, courtesy of Thales Alenia Space in Italy.

by fig. 2 and by the works [1,20,17], the NGGM can provide the scientific community with a gravitational tomography of our planet, resolving the ℓ, m dependence of the gravity field, particularly for that part related to the seismic cycle, such as the post-seismic and inter-seismic phases, not understood yet in terms of mass readjustment for earthquake magnitudes lower than 8.5–9.

5. – Gravity signals from a $M_w = 7.0$ scenario earthquake

This section is devoted to the presentatation of the gravitational effects of a scenario $M_w = 7.0$ normal fault earthquake, which could be considered representative of a strong

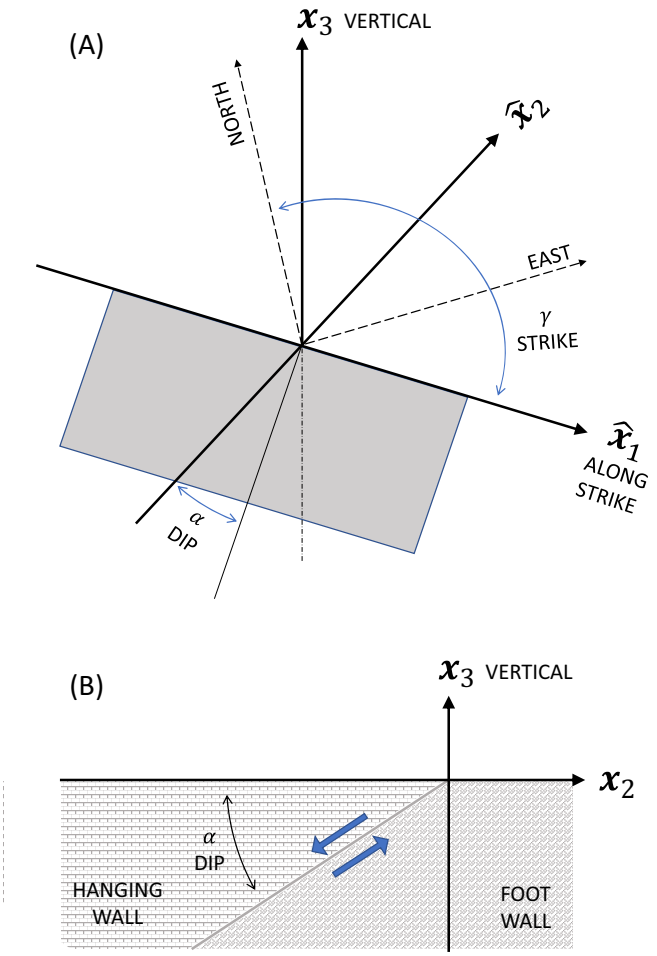

Fig. 4. – Characteristics of the fault for normal faulting, defining the angles of dip and strike. For the two cases under study the length of the fault is fixed at 45 km, the width at 30 km, the dip at 60°, the strike at 120°.

earthquake in Italy, once considered the $M_w = 6.9$ 1980 Irpinia earthquake. Normal faulting is associated with extensional tectonics, characterizing the deformation style of the central and southern Apennines, associated with the displacements of the external part of the Apennines towards the North- North-East direction compared to the inner part of the chain moving grossly to the North- North-West direction, slower than the external Adriatic part, as visible from GPS data [21] and from physical models predicting the horizontal strain and stress tensor, on the basis of the major tectonic forces in the Central Mediterranean, as the Africa-Eurasia continental collision and subduction underneath the Calabrian Arc [22,23]. The results are based on the fully realistic compressible Earth's model presented in sects. **1**–**3**.

The modelling of the post-seismic phase of a scenario $M_w = 7.0$ earthquake, comparable in magnitude with the 1980 Irpinia earthquake, provides a clear example regarding

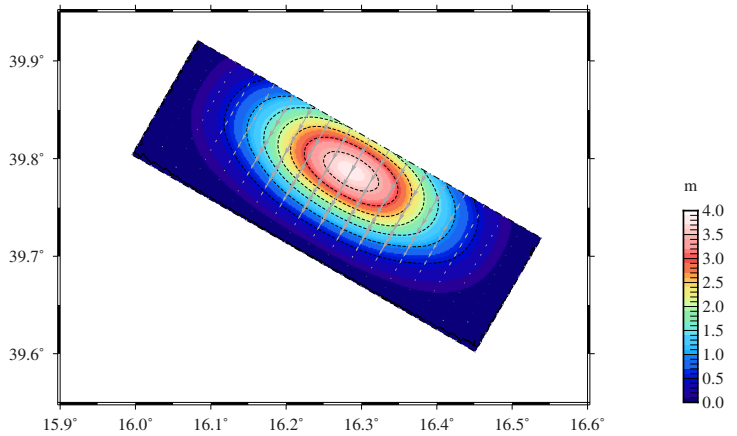

Fig. 5. – Shallow slip: slip over the fault, described by a biquadratic spline, for this shallow fault extending from 0 km to 26 km depth. The maximum slip is 3.8 m at 7.4 km.

the potential exploitation of the Earth's modelling presented in this work coupled with the NGGM data: vertical rates of the Earth's crust of the order of millimetres per year and wavelength of about 50 km, have been obtained by fitting vertical displacements from an old incompressible spherical model, building on the same methodology presented in sects. **1**-**2**, with levelling data [24]. This modelling provided the first demonstrable evidence of post-seismic effects in the Mediterranean following a normal fault earthquake within the frame of extensional tectonics. The post-seismic vertical displacements occurring over the 4 yr time span of the levelling campaigns carried out over the epicentral area are expected to produce a gravity signal which could nowadays hardly be visible with the current GRACE accuracy, suggesting that exploiting the incoming NGGM high-resolution data, in time and space, could make a step forward in our understanding of the physics of the seismic cycle within the frame of the herein self-gravitating Earth's models.

Figure 4 portrays the characteristics of the normal fault earthquake considered in this section, with the two blue opposite arrows on the two sides of the fault depicting the abrupt relative motion in extension during the earthquake, as for a normal fault; the angle of dip is defined as the angle between the fault's surface and the Earth's surface. In this figure the two portions of the crust overlying and underlying the fault are also defined in panel (B), named hanging wall and foot wall. The dip angle is fixed at 60°, dipping to the west, and this value is characteristic of normal faulting in the Apennines, but differs from that of the 1980 Irpinia earthquake, dipping to the east rather than to the west: this would not be responsible of any difficulty in the interpretation of the following results, since normal faulting dipping to the east would simple require, according to fig. 4, exchanging the positive and negative gravity values.

Figure 5 portrays the slip over the fault, described by a biquadratic spline which goes to zero at the edges of the fault, except for the shallow case in which the slip reaches the Earth's surface and differs from zero along the line of strike, which is 120° as specified in the caption of fig. 4. The mid point of the fault along the line of strike is at 16.31° E longitude and 39.82° N latitude. The largest slip at the hypocentre is 4 m, larger than the maximum 2.5 m inverted slip from levelling data of the 1980 Irpinia earthquake on the basis of an old incompressible model

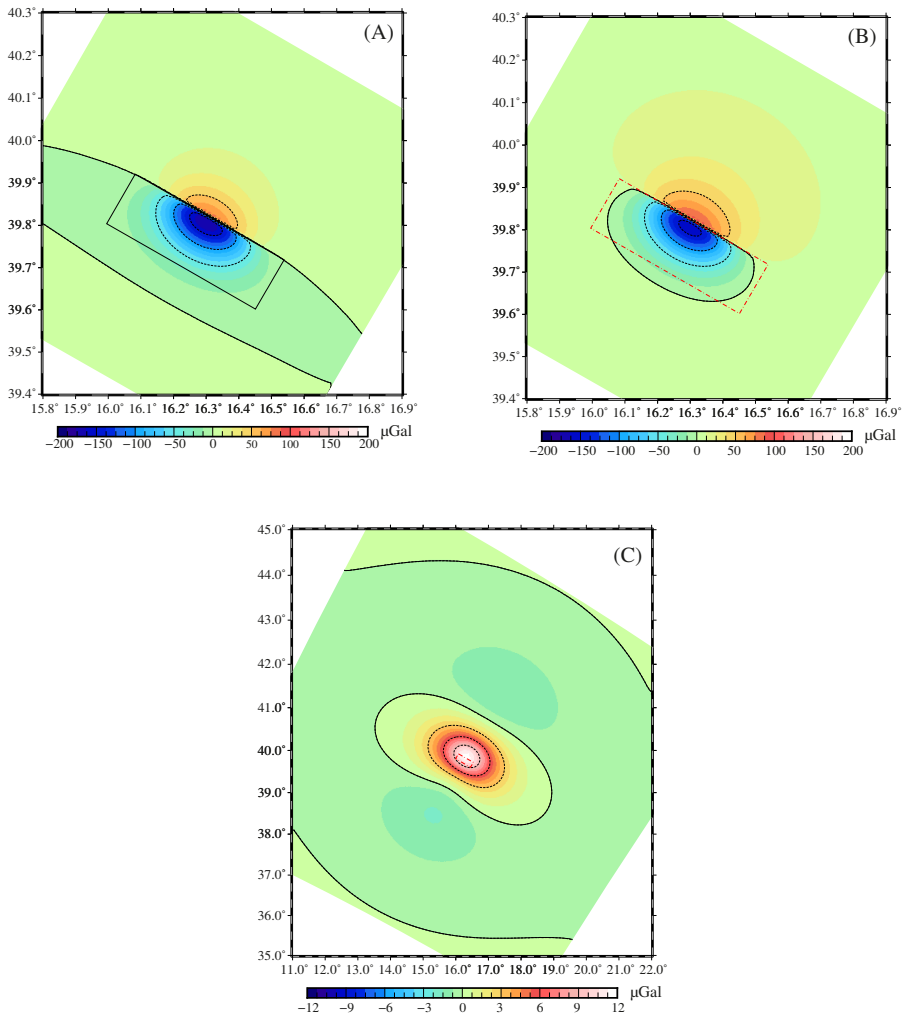

Fig. 6. – Shallow source, full resolution. Panel (A), co-seismic gravity anomaly, panel (B), steady-state gravity anomaly (after post-seismic displacement) and their difference, panel (C), in μGal.

Figure 6 shows the co-seismic gravity, or gravity anomaly, from the normal fault earthquake evaluated at the Earth's surface, in μGal, summing all the harmonics well beyond convergence, namely 500 000 harmonics: the top panel (A) represents the gravity signal of the earthquake when the Earth has reached its elastostatic equilibrium after the seismic waves have propagated, allowing the Earth to acquire a permanent elastic deformation. The solid rectangle represents the fault overprinted by the negative gravity anomaly and the black lines represent the zero, the transition between the negative anomalies, light green, to the positive ones, light yellow: comparison with fig. 5 indicates that the negative anomaly stands over the hanging wall, the portion of the crust over the fault in fig. 4, where the crust is subject to a general subsidence or downwarping, while a smaller positive anomaly overprints the footwall of the fault. The clear cut between

negative and positive values is caused by the fault reaching the Earth's surface and by the summation over such a large number of harmonics to guarantee that the gravity discontinuity at the fault's trace at the Earth's surface is well reproduced.

The gravity signal is characterized by a dipolar pattern, negative in the South-West and positive in the North-East, with respect to the clear cut at the edge fault reaching the Earth's surface, where the gravity anomaly is zero. The negative gravity anomaly is due to the downwarping of the Earth's crust, as also indicated by the down-dipping arrow in fig. 4 in the hanging wall, responsible for a layer of air substituting the crustal material at the Earth's surface and for the downwarping of the interfaces at depth between layers of different densities, with lighter material substituting heavier ones, finally ending into a mass deficit with respect to the situation before the earthquake occurrence. The positive gravity anomaly is on the contrary caused by the upwarping of the crust, with denser material substituting now lighter material, both at the surface and at depth. The peak-to-peak anomaly is about $200\,\mu$Gal, with the negative value larger by around a factor three with respect to the positive value, indicating that the downwarping of the crust is more important compared to the upwarping for a normal fault earthquake and that the upwarping is the flexural response of the crust to the downwarping.

The middle panel (B) represents the gravity anomaly at steady state, after post-seismic deformation has come to an end, so it includes the elastic contribution plus the viscous contribution due to stress relaxation of the viscoelastic material beneath the 50 km uppermost elastic layer. In this work we are not interested in the time evolution of the post-seismic gravity anomaly, but in the evaluation of the full post-sesismic gravity anomaly which is accumulated during the whole process of stress relaxation in the viscoelastic portion of the Earth below the elastic top layer of 50 km. In fact, we are interested in verifying whether the total amount of post-seismic gravity anomaly could become visible during the whole duration time of the NGGM space gravity missions, planned to be of about eleven years [1]. In terms of the Maxwell solid, steady state means that the shear relaxation function $q(t)$ in eq. (5) has fully relaxed, or that the time t is longer than the relaxation time τ. For the present case of a realistic compressible model based on the density and elastic stratification of the PREM [7], we lose to a certain extent the concept of viscoelastic normal modes as depicted in fig. 1 for a 5-layer incompressible Earth's model and representing the counterpart of the simple Maxwell solid of eq. (5). As we have explained in sect. **3**, the current realistic model is characterized by a richer spectrum of viscoelastic normal modes, including a continuous spectrum of modes in the Laplace domain requiring, as we have seen, a complex contour integration in the s-domain rather than the Residue Theorem, in order to include a denumerably infinite set of dilatational modes, compositional modes or even Raileigh-Taylor instability modes, as well as contributions from the continuous spectrum. The viscous contribution is about one order of magnitude lower than the elastic co-seismic contribution, as better seen in the panel (C) of fig. 6.

Comparing panel (B) with panel (A), it is striking that the area of light yellow representing a positive gravity anomaly widens with respect to the area of light green, meaning that there is a global gain of positive gravity anomaly, the latter appearing also in proximity of the negative and positive peaks, as made evident by the reduction of the area of negative anomaly and by an enlargement of the area of positive anomaly. Post-seismic deformation is thus responsible for a global increase of positive gravity anomalies, both locally and globally, and this is made evident in panel (C), which portrays the difference between panel (B) and panel (A).

Three findings are striking: the first is the smaller amplitude of the viscous signal by one order of magnitude compared to the co-seismic one, as made evident by the change in the gravity scales, the second is the broadening of the signal, now extending to distances of several times the length of the fault, as shown by the zero curve in panel (C) compared to panel (B) where the zero curve has dimensions comparable to those of the fault, the third is that for distances larger than the dimensions of the fault the gravity anomaly is positive, indicating a broad gain of mass centred over the epicentral area. In order to understand this third finding, we need to remind that the fault in extension is located above the neutral plane of the 50 km thick outermost elastic layer, which is responsible for the smooth upwarping when the final configuration of the elastic layer is sustained solely by the elastic stresses stored in the plate, after full relaxation took place underneath.

At full resolution, post-seismic deformation is responsible for a positive gravity anomaly of 12 μGal, about a factor 17 smaller than the elastic co-seismic contribution. Depending on the viscosity of the mantle layer underneath the elastic one, post-seismic deformation could occur on time scales ranging from years to thousand years, but it is obvious that the time scale that could be relevant for the NGGM gravity missions ranges from months to years and decades, since this mission is supposed to fly for about eleven years. The time scales portrayed by fig. 1 range from 10^2 to 10^5 yr for the relevant modes (except the transient T ones) and for the harmonic degree $\ell = 2$, which is the mode containing the widest interval in time scales, with the $\ell = 10, 100$ ones contained in this interval: these values are obtained for a reference mantle viscosity of 10^{21} Pa s which is too stiff to be relevant for post-seismic deformation and represents in fact the mantle viscosity which is obtained in Post Glacial Rebound studies [25, 26] or in mantle convection simulations [27]. These time scales move to shorter ones for realistic viscosities of the asthenosphere of about 10^{18}–10^{19} Pa s or for viscosities of the transition zone in the crust, sandwiched between the brittle top elastic crust and the stiffer lower crust, characterized by viscosities that can well be of the order of 10^{18} Pa s, so that the post-seismic gravity anomaly can reach its final steady-state value over a few years or few decades, well within or comparable in the slowest case with the flight time of the NGGM.

Concerning the detectability of the gravitational time-dependent post-seismic signal, we have to model the latter in the NGGM bandwidth, up to 250 spherical harmonics, or 160 km wavelength, which means a resolution of 80 km (half-wavelength) as for GOCE in space and around 1 μGal/yr as for GRACE in time. In fig. 7 we thus portray the gravity anomaly patterns at the GOCE spatial resolution, which means summing over 250 harmonics and reaching a spatial resolution of 80 km (half-wavelength). For compensating the poorly known short-wavelength spherical harmonic coefficients, we also apply the Jekeli's Gaussian filter [28] of radius $R_W = 80$ km (see appendix A for details).

Comparison of the (A) panels of figs. 6 and 7 shows that the co-seismic signal is subject to a substantial decrease of about two orders of magnitude at the GOCE resolution compared to the full resolution, which is not the case for the viscous contribution. In fact, comparison of the (C) panels of these two figures, and comparing both with the (B) panel of fig. 7, shows that the positive viscous contribution is reduced only by a factor three, from 12 to 4 μGal, when passing from the full to the 80 km spatial resolution. At the GOCE resolution, and for this scenario earthquake where viscoelastic relaxation occurs at the depth of 50 km, the viscous post-seismic contribution is better resolvable than the elastic co-seismic one, and is in principle resolvable by the NGGM, once the peak-to-peak value of about 5 μGal, from the white to the light blue in panels (B) or (C) in fig. 7, is gained over the flight duration of the gravity mission. The dipolar co-seismic

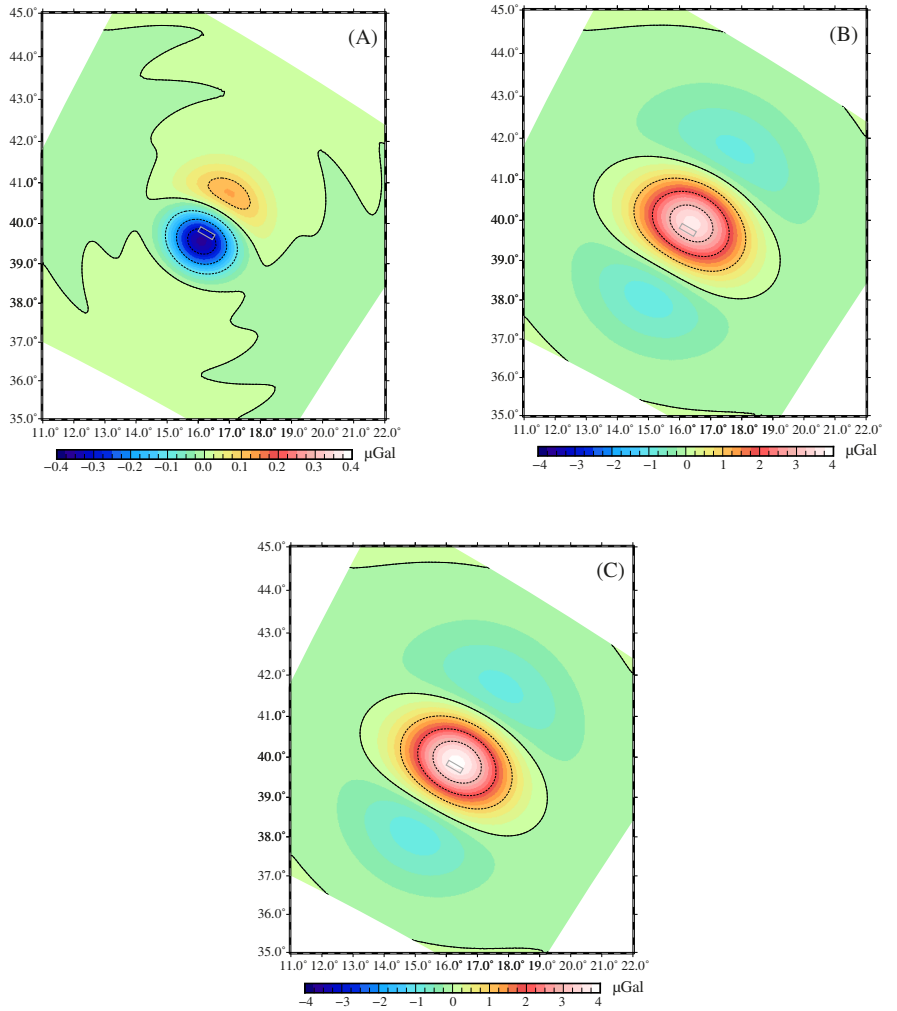

Fig. 7. – As in fig. 6, but at GOCE resolution.

pattern is maintained also at the GOCE spatial resolution, and the arguments raised when discussing fig. 6 regarding the post-seismic pattern are valid also for fig. 7.

This behaviour is confirmed, and even strengthened, when the GRACE spatial resolution is considered in fig. 8, summing up to spherical harmonic degree $\ell = 90$ and after spatial average with the Jekeli's Gaussian filter [28] of radius $R_W = 300\,\mathrm{km}$ (see appendix A for details). The co-seismic signal of panel (A) is largely broadened with respect to the full-resolution case of fig. 6, or even with respect to the GOCE case. The co-seismic pattern, although reduced to $0.1\,\mu$Gal, portrays a well-shaped dipolar pattern. It is interesting to note that the viscous contribution, of about $2.5\,\mu$Gal, is reduced by a factor two with respect to the GOCE case. Both at the GOCE an GRACE resolution, the post-seismic signal is foreseen to be resolvable at the NGGM spatial and time resolution, better than the co-seismic contribution, when viscous relaxation occurs as in this case below the elastic crust. The findings from figs. 6–8 indicate that gravity missions at

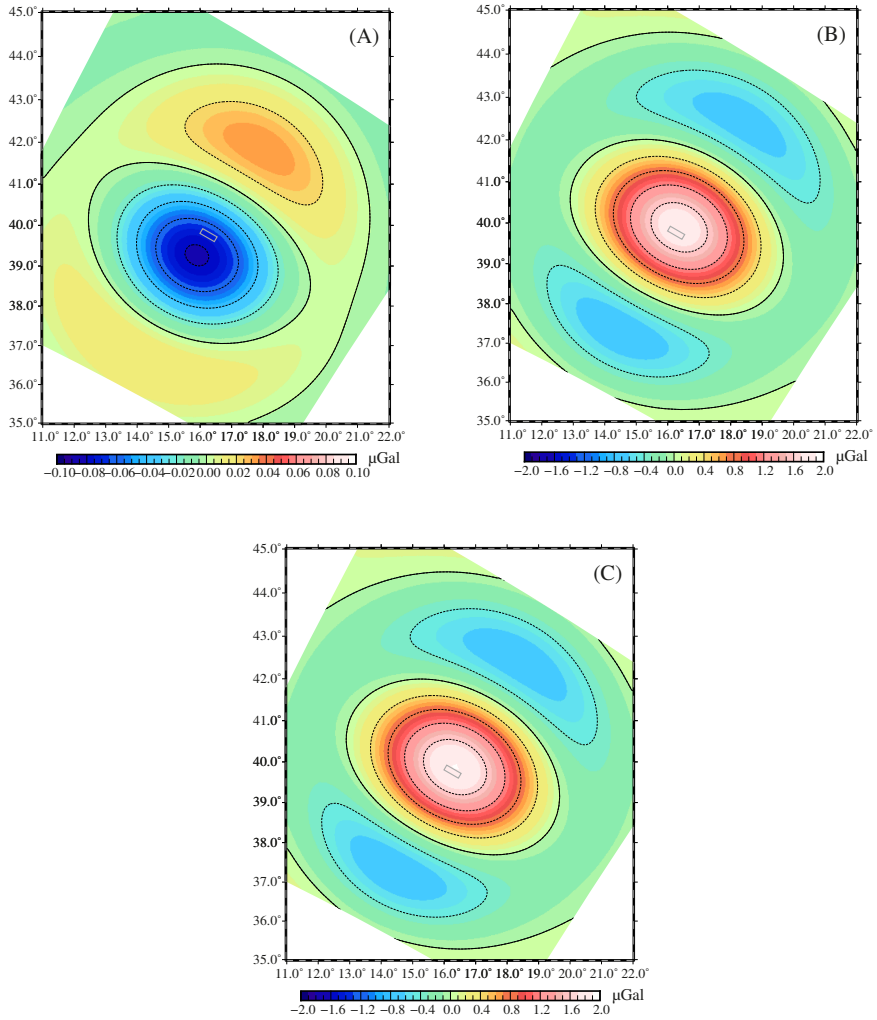

Fig. 8. – As in fig. 6, but at GRACE resolution.

the GOCE spatial resolution and at the GRACE time resolution are expected to sample the post-seismic deformation better than the co-seismic deformation. The broadening of the post-seismic pattern compared to the co-seismic one enriches in fact the wavelength content in the NGGM bandwidth, since viscous relaxation involves layers of the Earth deeper than the top elastic crust where the source is located, so triggering longer wavelengths compared to those from co-seismic deformation.

In this contest, it is interesting also to consider the effects of deepening the seismic source, which is expected to trigger longer wavelengths once comparing with a shallow source as in figs. 5–8. Figure 9 shows the slip distribution of the seismic source as in fig. 5, but deepened by 10 km and going to zero at the top edge being now fully embedded within the Earth. Figures 10–12 represent the counterparts of figs. 6–8, but for this deeper source.

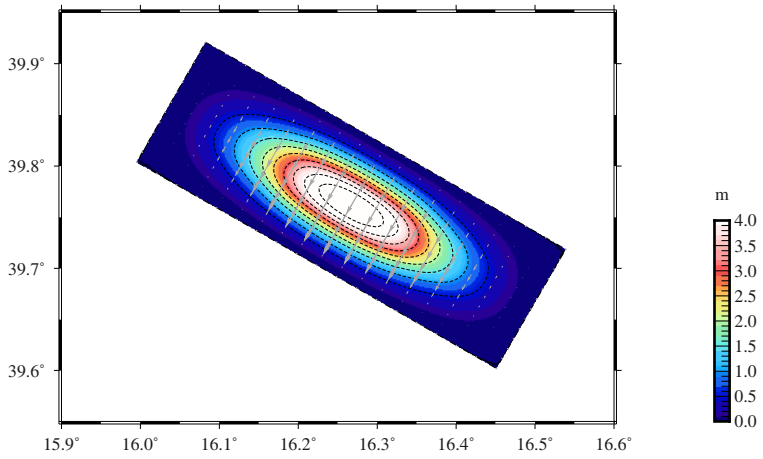

Fig. 9. – Deep slip: slip over the fault, described by a biquadratic spline, for this fault extending from 10 km to 36 km depth; the maximum slip is 5 m at 23 km depth.

The full resolution fig. 10, panel (A), shows that the deepening of the source has a twofold impact on the co-seismic dipolar gravity anomaly, by reducing by about a factor three the amplitude of the anomaly, now within the scale of 60 μGal and by widening by about the same amount the surface anomaly signature. The viscous relaxation gravity signal overprints the co-seismic signal by increasing the positive gravity anomaly and by decreasing the negative one, without affecting the lateral dimension of the pattern. Panel (C), representing the only viscous contribution, is resembling the viscous contribution from the shallow source of fig. 6, in terms of characteristic wavelength and amplitude, about 12 μGal, which is not surprising since, once triggered, the viscous contribution is controlled by the depth of the relaxing viscoelastic layer, the same in figs. 6 and 10; we note only a slightly reduced flexural response represented by the gravity decrease in the southwest with respect to the positive maximum. The deepening of the source has instead a major effect on the amplitude and wavelength of the co-seismic gravity anomaly.

When we move to fig. 11 GOCE resolution, we note that the decrease in the gravity signal from full and GOCE resolution for the deep source is not as large as for the shallow source, which is physically sound since the deepening of the source enriches the longer-wavelength content compared to the shallow source as shown by the pattern enlargement of panel (A): compared to the shallow source, the reduction from the GOCE resolution compared to the full case is about a factor sixty rather than about two hundreds. The GOCE resolution post-seismic signal is reduced by about a factor two compared to the shallow source GOCE case. The ratio between the post-seismic to co-seismic signal is 2.5 for the deep source GOCE case, compared to 10 for the shallow case, which also indicates the enrichment of long-wavelength content in the co-seismic gravity signal when the source is deep.

Panel (C), fig. 11, confirms this finding at the GRACE resolution, fig. 12, panel (C), although the ratio between the post-seismic and co-seismic gravity contributions is about doubled compared to the GOCE resolution case.

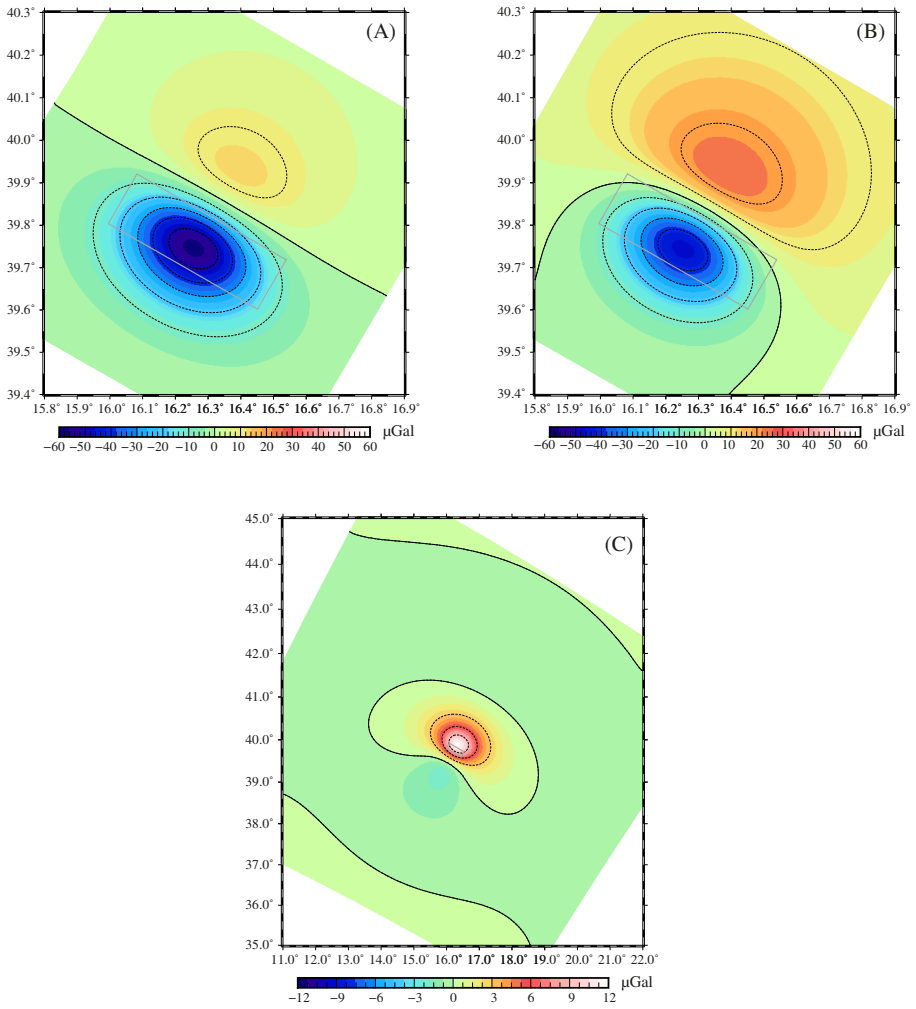

Fig. 10. – Deep source, full resolution. Panel (A), co-seismic gravity anomaly, panel (B), steady-state gravity anomaly (after post-seismic displacement) and their difference, panel (C), in μGal.

6. – Gravity signals from large earthquakes at subduction zones

This section is devoted to the presentation of results regarding the large 2004 Sumatran earthquake which prove the capability of gravitational seismology to constrain the mass readjustment at large depths, from the ocean overlying the epicentral area to the uppermost portion of the Earth's mantle.

The analysis of GRACE Level 2 data time series from the Center for Space Research (CSR) and GeoForschungsZentrum (GFZ) performed in [29], allowed us to extract the co-seismic gravity signal caused by the 2004 Sumatran earthquake, based on the compressible self-gravitating Earth model described in sects. **1**–**3** and including the gravitational effects of the sea level feedback, namely the redistribution of the ocean water during

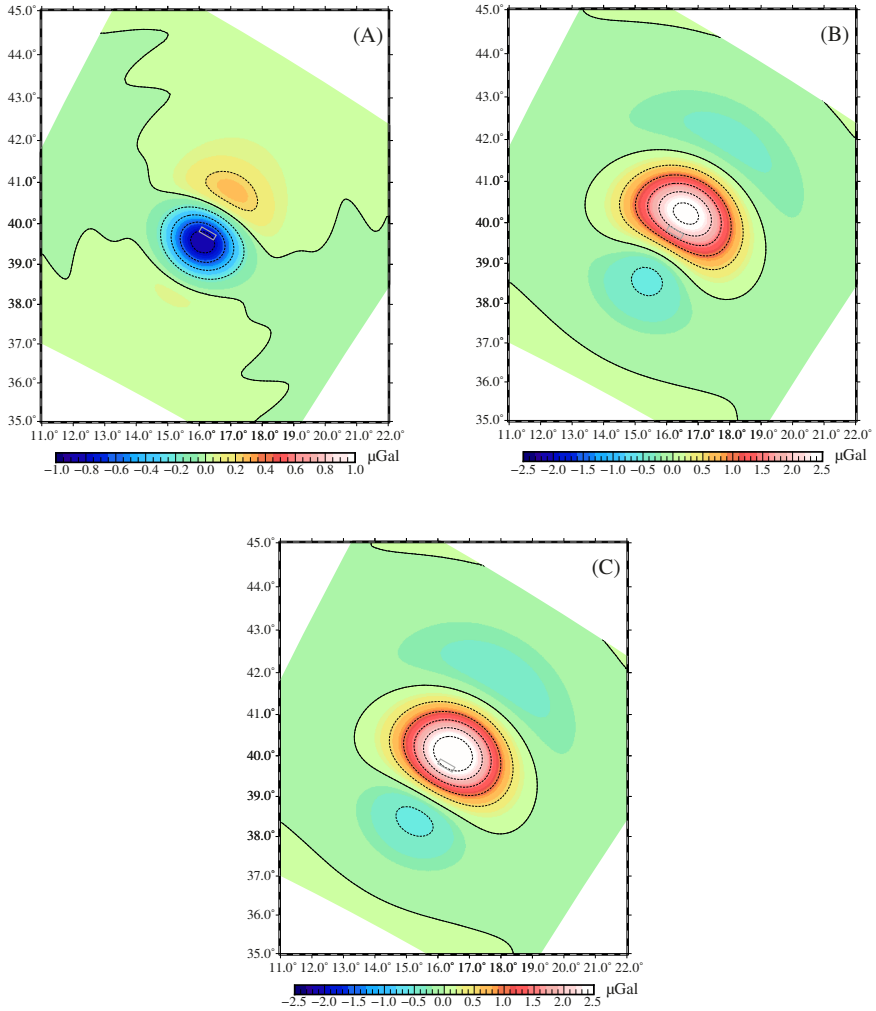

Fig. 11. – As in fig. 10, but at GOCE resolution.

the co-seismic deformation of the ocean bottom in the epicentral area. The 2004 Sumatran earthquake has a magnitude $M_w = 9.3$, and is thus among the largest earthquakes ever recorded since the beginning of the instrumental seismology. The mechanism of this earthquake is opposite to the normal fault scenario earthquake considered in the previous section, since it is associated to the compression of the Earth's crust, rather than its extension, at the subduction zone where the oceanic lithosphere of the Indian Ocean subducts, or penetrates within the mantle, underneath the Eurasian continental crust in the Sumatran region. In this section, instead of considering as case study a $M_w = 7$ scenario earthquake purposely designed for providing the synthetic gravity pattern for the incoming NGGM, we show the observed GRACE gravity pattern produced by a real earthquake, demonstrating that this kind of gravitational data can be used to estimate the mass readjustment at great depth in the Earth during the occurrence of the earthquakes, thus allowing us to make a step ahead in our understanding of the physics of the earthquakes.

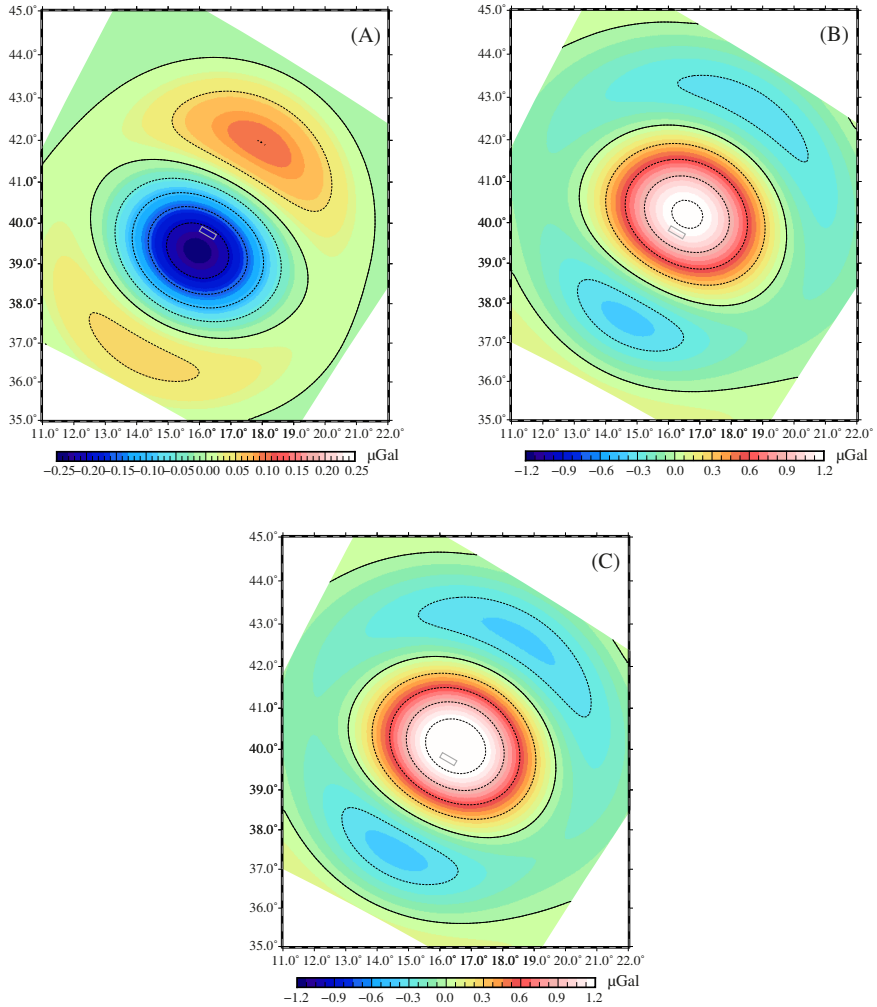

Fig. 12. – As in fig. 10, but at GRACE resolution.

Figure 13 shows the co-seismic gravity jump and the linear trends extracted from GRACE data after the 2004 Sumatran earthquake overprinting the Sumatra and Thailand geography, sampling the Sumatran region every 1.4°. In this case, GRACE gravity data have been averaged in space using the DDK3 anisotropic filter [30] that is comparable with the Jekely's Gaussian filter [28] of radius $R_W = 220\,\mathrm{km}$. From the original time series fitting, panel (a), we obtain a maximum co-seismic gravity anomaly of $+7.5\pm0.6\,\mu$Gal, and minimum, $13.1\pm0.8\,\mu$Gal at the points $(95.6°, 0.7°)$ and $(97.0°, 7.7°)$. These estimates differ by less than 4 per cent from the maximum, $+7.5\pm0.6\,\mu$Gal, and minimum, $12.7\pm1.0\,\mu$Gal, gravity values obtained at the same points from the smoothed time series fitting, as in panel (c).

The strike of the normal $M_w = 7$ scenario earthquake of the previous section is 120° while that of the Sumatran fault is 343° as obtained by [31], dipping with different an-

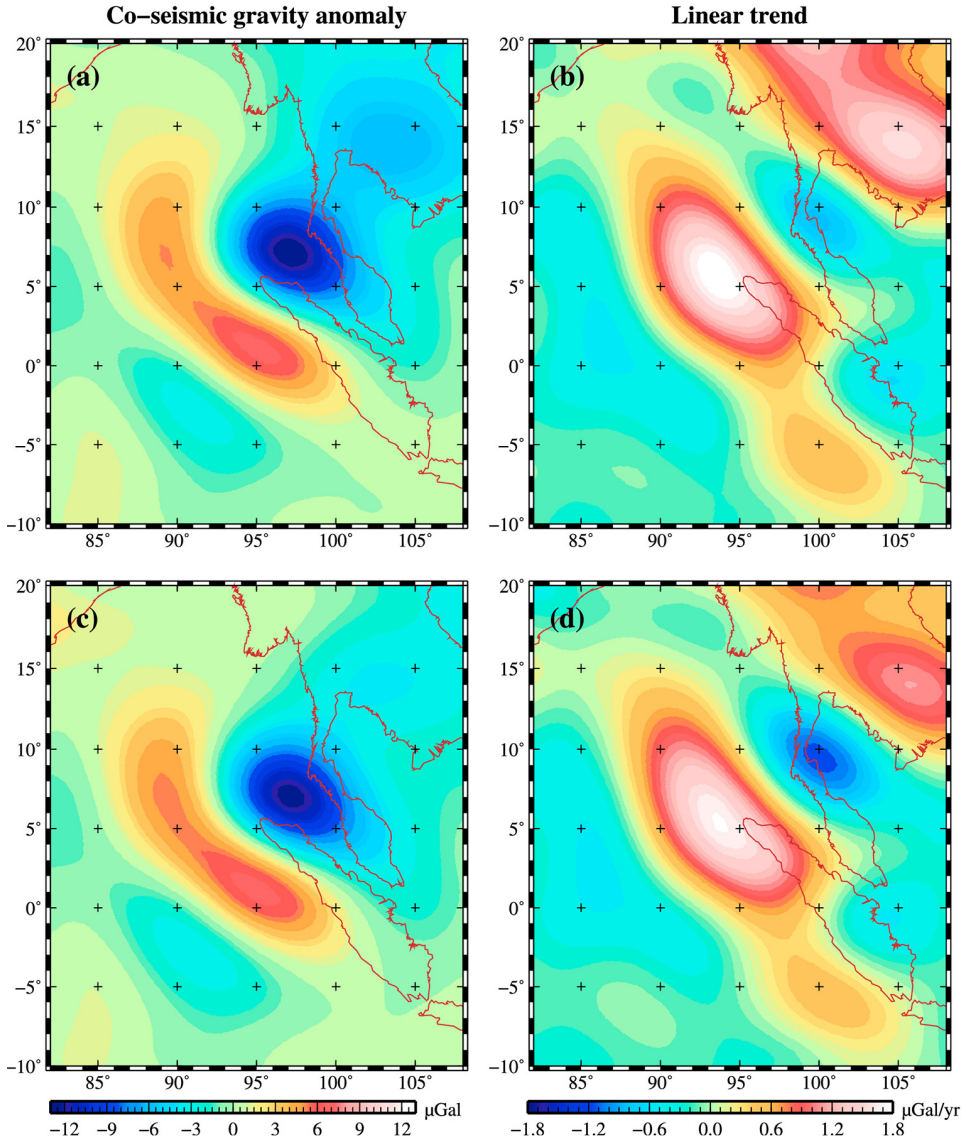

Fig. 13. – Co-seismic gravity anomalies and linear trends obtained by linear fitting to the original GRACE data, panel (a) and (b), and smoothed GRACE data time series, panel (c) and (d), for the 2004 Sumatran earthquake. This figure is fig. 6 of [29].

gles, about 60° to the West for the normal fault and varying from about 13° at shallow depths to about 30° to the East at large depths for the Sumatran earthquake. Such a large difference in the dip of the faults is of course a consequence of the two different tectonic styles, the slow extensional one of the Apennines and the fast converging one of the Sumatran region. Regarding fig. 4, if we want to visualize the relative motion of the two parts of the fault for the Sumatran earthquake, we have to reverse the two arrows and the fault immersion at low angles to the right rather than to the left in order

to account for the thrust earthquake occurring at the interface between the subducting oceanic Indian plate converging towards the continental Eurasian plate, at rates of about 7 cm/yr. This high convergence rate, responsible for the $M_w = 9.3$ 2004 Sumatran thrust earthquake, should be compared with the extensional rates in the southern Apennines of a few millimetres per year, in order to realize why at fast converging subduction zones earthquakes of magnitudes as high as $M_w = 9$ can be generated, compared to lower magnitudes $M_w = 6$–7 normal fault earthquakes at slow extensional tectonic environments. If we reverse the relative motion between the two parts of the fault, then we can understand why the gravity patterns of figs. 6–8 and 9–12 portray an inverted polarity, with negative gravity anomaly, blue, in the South-West and positive gravity anomaly, red, in the North-East for the normal fault of figs. 6–8 and 10–12, and reversed colours for the thrust earthquake of fig. 13. Figure 4 shows that the portion of the crust in the South-West is subject to subsidence, which produces a mass deficit, since dense crustal material of about 2750 kg/m^3 is substituted by air, and then the blue gravity low, while in fig. 13 the opposite motion of the Indian and Eurasian portions of the crust are responsible for the upwarping of the crust in the southern part of the Eurasian plate overriding onto the Indian one, which causes a mass excess and thus a positive gravity anomaly, red. The negative gravity anomaly in the North-East is caused by the water of the Indian ocean, which leaves the epicentral region, being displaced away from the epicentre by the tsunami, thus causing a mass deficit and a gravity low, combined with the flexural response of the Eurasia plate, downwarping in the North-East, with a mass deficit now contributing to the gravity low together with the mass deficit left by the tsunami.

Panels (b) and (d) of fig. 13 represent the rate of gravity change in μGal/yr associated to the post-seismic deformation after the co-seismic one, providing a value of about 3.5 μGal/yr from peak-to-peak. It is interesting to compare this post-seismic pattern at the GRACE spatial resolution with the post-seismic pattern given in panels (C) of figs. 7 and 11, providing the whole post-seismic gravity contribution from the normal fault $M_w = 7$ scenario earthquake at the GOCE spatial resolution, coinciding with the spatial NGGM resolution, of about 3–4 μGal peak-to-peak, depending on the source depth, accumulated during the whole post-seismic history, which means that the rate of gravity change will depend, as stated in the previous section, on the viscosity of the layers where stress relaxation occurs. Although these two post-seismic contributions cannot be directly compared, these findings indicate that GRACE has demonstrated the capability to detect the post-seismic gravity change, of the order of several μGal per year for huge earthquakes of magnitudes of about $M_w = 9$. If the 3–4 μGal is accumulated over time scales of years, the NGGM are expected to detect the post-seismic gravity changes from earthquake magnitudes as low as $M_w = 7$ at the GOCE spatial resolution, being around 1 μGal/yr the expected accuracy in the gravity NGGM measurements at the same spatial resolution of the GOCE mission.

This mass readjustment, contributing to the gravity minima and maxima as shown in the GRACE data of fig. 13, can be better understood by watching the results of figs. 14–16, where the gravity effects of the mass rearrangements in the different parts of the planet are portrayed, including the gravity low due the mass deficit of the ocean water washed out from the epicentral region by the tsunami as shown in fig. 16.

Instead of fig. 13 observational results, fig. 14 shows the modeled contributions to the gravity anomaly, based on the seismological solution by [31] to constrain the fault parameters and smoothed according to the GRACE spatial resolution, resulting from the different parts of the Earth at different depths during the co-seismic deformation, from

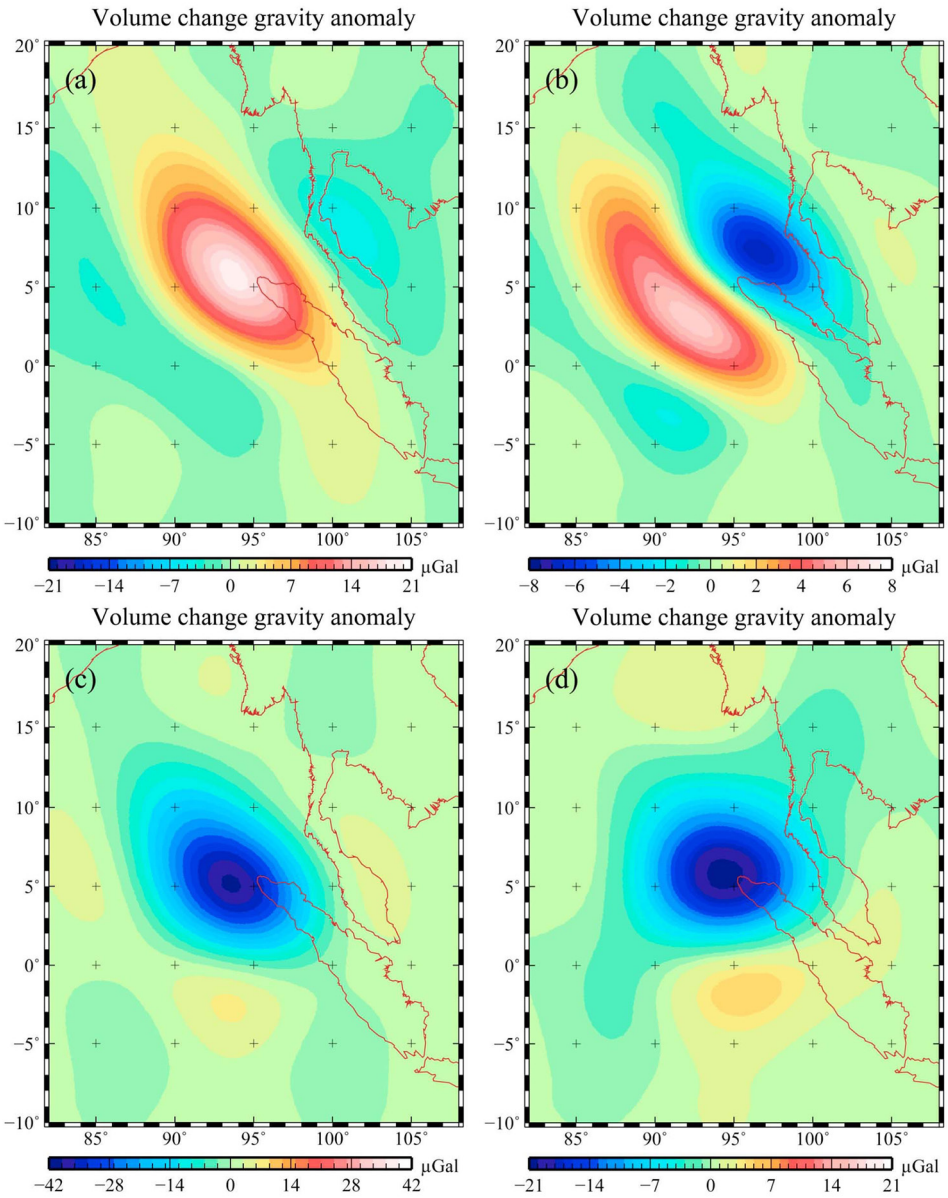

Fig. 14. – Filtered co-seismic gravity anomalies for compressible O-PREM, including a uniformly thick ocean overlying the Solid Earth PREM as in [7], due to volume changes of the mantle, panel (a), of the crust, panel (b), and due to the volume changes localized at the fault discontinuity, panel (c), obtained using the seismic source model of [31] modified as discussed in [29]. Panel (d) provides the gravity anomaly pattern due to the sum of the previous panels (a)–(c). This figure is fig. 11 of [29].

the mantle to the surface: these contributions are obtained by means of our compressible, self-gravitating model described in the previous sections. These results include the effects of the ocean water redistribution within a PREM model overlayed by an ocean of uniform

thickness, which is thus named O-PREM standing for Ocean-PREM, and are obtained by fitting our model with the co-seismic GRACE data of fig. 13.

The [31] solution is based on the Centroid Moment Tensor (CMT) analysis of the 2004 Sumatran earthquake, with five point sources used in the inversion to reproduce the propagating slip. These five point sources are visualized in fig. 1 of [31]. The geographical distribution of these five sources follows the arcuate geometry of the subduction trench and the average strike of the sources is 343°: the largest seismic moment release is provided by the point source facing the northernmost part of the Sumatran island, with the five sources following the shape of the arcuate island arc, north of Sumatra.

Panel (a) shows the effects on the gravity due to volume changes in the mantle (from the core mantle boundary, at 3485 km from the Earth's centre, to the bottom of the crust), although the localized positive gravity anomaly indicates that the volume changes occur in the uppermost part of the mantle down to depths comparable with the lateral extension of the anomaly of the order of a few hundred kilometres downward from the bottom of the crust. The positive gravity anomaly indicates a mass excess, which means that the mantle material is being compressed underneath the epicentral area, as expected for convergence and thus crustal shortening in the horizontal direction and widening the vertical direction: this process causes the downwarping of the crust-mantle interface and thus the compression of the mantle.

Panel (b) of fig. 14 shows the gravity anomaly due to the co-seismic volume changes in the crust, not including the effects in proximity of the fault, characterized by a maximum of 6.6 μGal in the South-West and a minimum of 7.0 μGal in the North-East. This dipolar gravity pattern indicates that the volume changes due to a thrust earthquake, such as the Sumatran earthquake, cause both compression and dilatation within the crust, in concordance with the seismic radiation pattern from thrust earthquakes. When we consider the effects of volume changes of the crustal material localized at the fault discontinuity in panel (c), we obtain a large dilatation, characterized by a minimum of 40.7 μGal: this dilatation is caused by the abrupt de-compression of the crust when it is unlocked by the earthquake. The evaluation of the gravity effects from the volume changes in proximity of the fault separately from those occurring in the crust not including the gouge of the fault, allows to correctly obtain the deformation style within the crust as in panel (b), which includes compression within the subduction oceanic lithosphere.

By considering the total contribution in panel (d) from the co-seismic volume changes of the mantle, panel (a), and of the crust, panel (b), together with the large dilatation localized at the fault discontinuity of panel (c), we predict a gravity pattern characterized by two maxima southwards, 5.3 μGal, and northward, 2.9 μGal, with respect to a more pronounced minimum of 21.5 μGal, in the near field of the Sumatran earthquake. In fig. 14 we demonstrate the importance of discriminating the effects of the co-seismic volume changes in the different layers of the Earth from the dilatation localized at the fault discontinuity. Otherwise, since the dilatation at the fault dominates over the volume changes effects in the crust, we would erroneously conclude that thrust earthquakes cause an overall dilatation of the crust, which is not physically sound because it does not reflect the pattern of compression and extension induced by the seismic forcing as also enlightened by the seismic radiation from a thrust earthquake.

Beyond the above considerations, the analysis of fig. 14 is meaningful because it shows that contributions to gravity anomalies due to co-seismic volume changes of the mantle and of the crust are important, being comparable with the full co-seismic gravity anomaly values, as those from the observational data of fig. 13. This indicates that compressibility

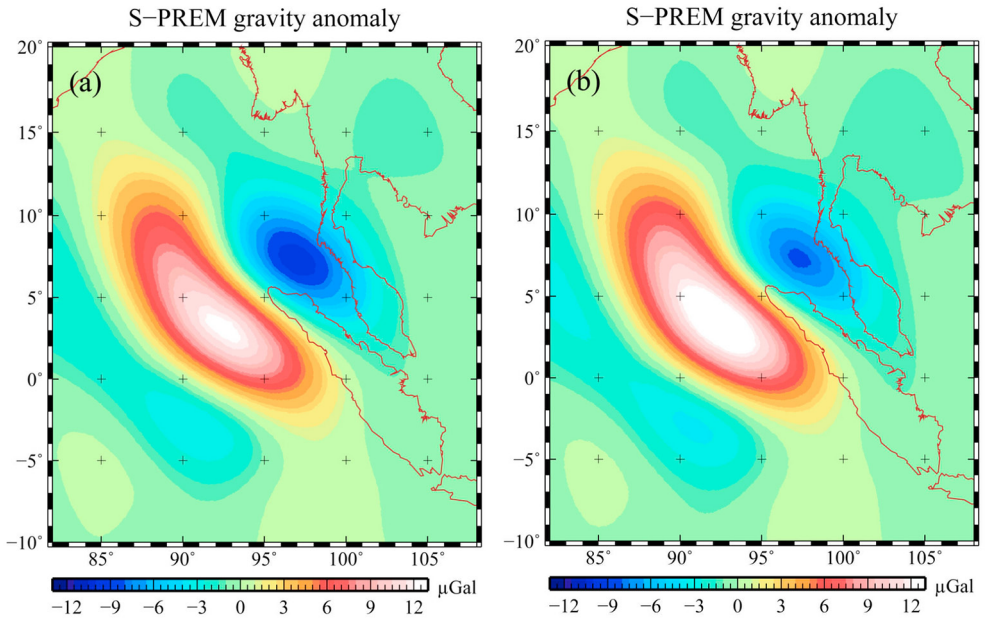

Fig. 15. – Filtered co-seismic gravity anomalies for compressible, panel (a), and incompressible, panel (b), S-PREM, obtained using the seismic source model of [31] modified as discussed in [29]. This figure is fig. 12 of [29].

is an important physical characteristics of the co-seismic gravity perturbations. It is thus important to exploit further the effects of compressibility by comparing compressible and incompressible Earth models in order to analyze in detail the role of compressibility on the earthquake physics, as done in fig. 15.

In fig. 15 we compare the smoothed co-seismic gravity anomalies for compressible, panel (a), and incompressible, panel (b), models, where the S-PREM stands for the complete Solid Earth processes without the ocean as in O-PREM, including the effects of both volume changes and gravity signals from interface displacements where the density is discontinuous, as for example the Earth's surface and the Moho discontinuity between the crust and the mantle. Compared to fig. 14, fig. 15 thus includes the effects of the topography perturbations, where materials of different densities, as those of the mantle, the crust and the air, are displaced. The peak-to-peak gravity anomalies are 22.8 and 23.4 μGal, for compressible, panel (a), and incompressible, panel (b), Solid Earth models, without the effects of the ocean. The two bipolar patterns are asymmetric toward the positive co-seismic gravity anomaly, particularly in the incompressible case. By comparing panel (a) of fig. 15 with panel (c) of fig. 14, we visualize the effect of the surface topography included in panel (a), which increases the positive gravity values in the South-West, thanks to the upwarping of the crust: the effect of the surface topography is thus to make the S-PREM model more similar to the observed co-seismic gravity pattern of fig. 13 compared to those of fig. 14, not including the gravity effects from the surface topography. Comparing figs. 13 and 15, we note that in the observational data the negative gravity values are larger in magnitude than the positive ones, opposite to the findings from fig. 15: in order to bring into concordance model predictions and observations, we must include the effects of the ocean, as in fig. 16.

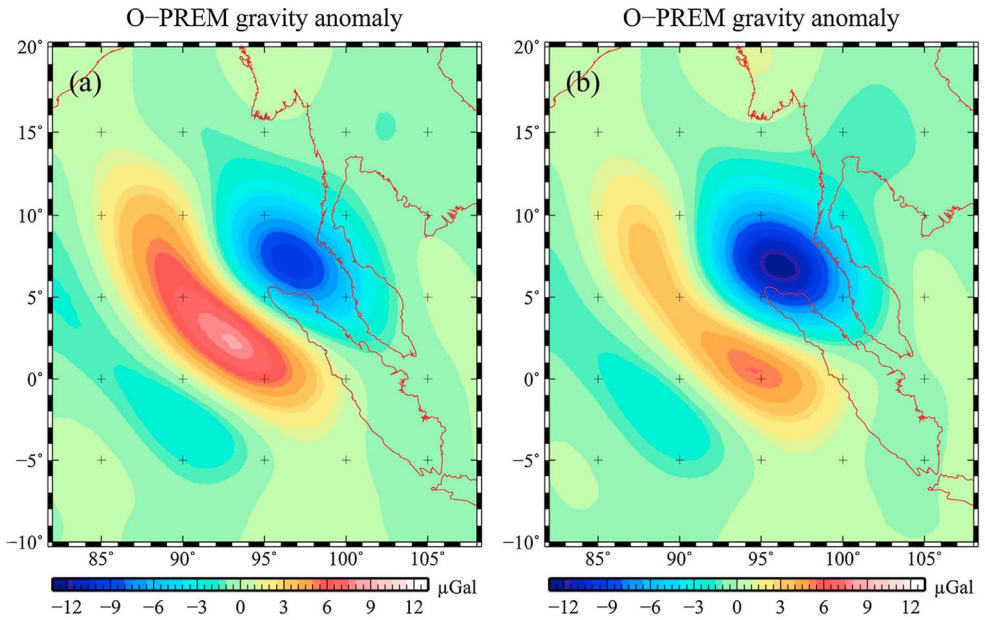

Fig. 16. – Filtered co-seismic gravity anomalies for compressible O-PREM obtained using the (a) original and (b) modified seismic source models of [31], with source depths below, 25 km, and above, 15 km, the Moho discontinuity, respectively. The dip angles for the modified seismic source models have been increased by 50 per cent. This figure is fig. 9 of [29].

We show in fig. 16 the co-seismic gravity anomalies obtained from the compressible O-PREM model, which includes the effects of the ocean water redistribution, different from the panel (a) of fig. 15 regarding the compressible S-PREM model accounting solely for the effects of the Solid Earth; panel (a) and (b) of this figure refer to two slightly different versions of the seismological solution used to build the forcing associated to the earthquake. In particular, panel (a) includes the sea level feedback and is based on the seismic source model of [31], after smoothing. We find maximum, $+8.6\,\mu$Gal, and minimum, $10.0\,\mu$Gal, gravity anomalies at points $(92.8°, 2.1°)$ and $(97.0°, 6.3°)$. The peak-to-peak gravity anomaly obtained from the model, $+18.6\,\mu$Gal, is in agreement, within one-sigma error, with the observed one, $+18.8 \pm 1.7\,\mu$Gal, while the asymmetry coefficient AS representing the ratio between the maximum and minimum gravity values, the latter changed in sign, is 1.2 and differs from the observed one, $\mathrm{AS} = 2.1 \pm 0.5$, by about two-sigma error. Panel (b) portrays the co-seismic gravity anomalies for the compressible O-PREM obtained using a modified version of the seismic source models of [31], in which the source depth has been reduced with respect to panel (a). In this case, although the peak-to-peak anomaly remains constant, the gravity pattern, with the amplitude of the minimum larger than that of the maximum, is in accordance with the observed pattern of fig. 13.

Material compressibility plays a crucial role in the modeling of the sea level feedback of the O-PREM models, as shown in fig. 17, where we compare the co-seismic gravity anomalies due to the sea level feedback of compressible, panel (a), and incompressible, panel (b), models. Indeed, for the compressible case, the sea level feedback is responsible for a large negative gravity anomaly in the near field, with a minimum of $10.7\,\mu$Gal.

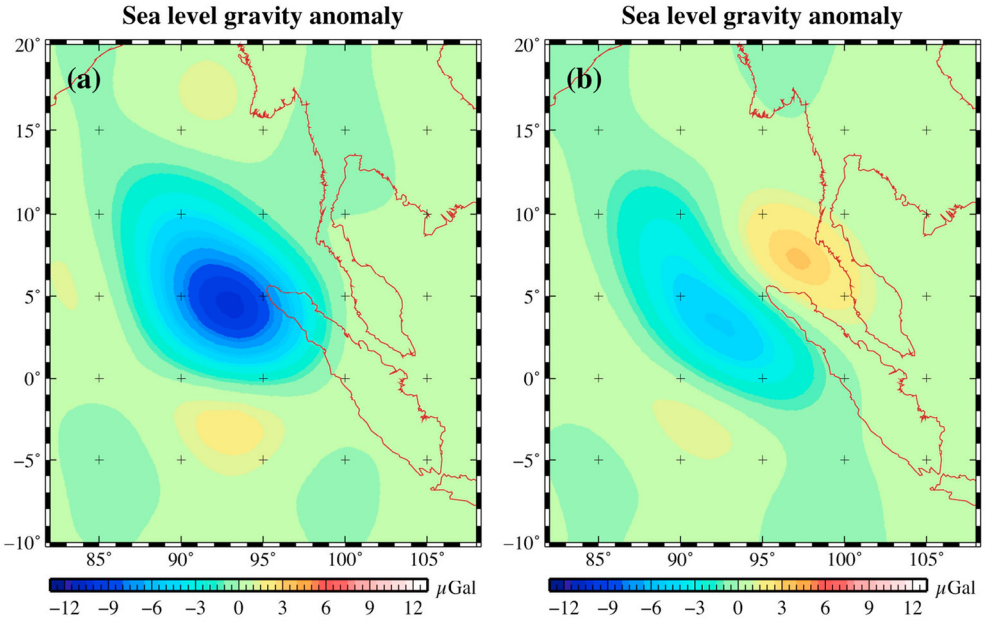

Fig. 17. – Filtered co-seismic gravity anomalies due to sea level feedback obtained by subtracting (a) compressible and (b) incompressible O-PREM and S-PREM co-seismic gravity anomalies and by using the seismic source model of [31] modified as discussed in Cambiotti *et al.* [29]. This figure is fig. 14 of [29].

These panels are obtained by subtracting the gravity patterns of the O-PREM models, for example the O-PREM model of fig. 16, panel (a), from the corresponding Solid Earth models S-PREM of fig. 15. For the incompressible case, the sea level feedback causes co-seismic gravity anomalies characterized by a bipolar pattern, with maximum and minimum of 3.3 and 5.3 μGal, respectively, which is opposite to the bipolar pattern of the co-seismic gravity anomalies of the incompressible S-PREM, fig. 15 panel (b). This means that the sea level feedback obtained from incompressible models reduces the magnitude of the maximum and minimum co-seismic gravity anomalies, thus reducing the peak-to-peak gravity anomaly, and does not explain the spatial asymmetry observed in GRACE data, where the gravity low is larger in magnitude than the gravity high.

The combined effects of the volume changes due to compressibility and those of the ocean water redistribution, or ocean feedback, with the water leaving with the tsunami the region of the uplifted ocean bottom, is responsible for the observed asymmetry of the observed gravity pattern recovered from GRACE data at Sumatra.

7. – Conclusions

The re-analysis of the already published results (which appeared in [29]) of the previous sect. **6**, as well as the findings from other authors, as Han *et al.* [32]; de Linage *et al.* [33], show that the gravity anomalies caused by large thrust earthquakes at subduction zones, with magnitude larger than $M_w = 8.5$–9.0, can reveal a new physics, beyond the possibilities of the classical seismology based on wave propagation. In fact, Gravita-

tional Seismology is based on the detection from space of the gravity signals arising from mass readjustment, rather than from displacements at seismometers localized essentially over lands. First of all, gravity space missions can detect signals over areas not covered by seismometers, as in the oceans, thus providing a uniform coverage in the data acquisition and fruitfully complementing the classical seismology. The discussion of the 2004 Sumatran results carried out in sect. **6** demonstrates this point very clearly, since when data analysis is complemented by the adequate modelling as discussed above and as detailed in [29], we can extract information that would be impossible to obtain from other methodologies. These new results and this new physics has been made possible by the compressible, self-gravitating Earth model described in the present study, which is fully realistic as it builds on the seismological Preliminary Reference Earth Model [7]. Our approach differs from that followed by [34] and [33], who used compressible models based on a free-oscillation scheme. It is worthwhile to emphasize that, in order to obtain the results of sect. **6** on the 2004 Sumatran earthquake regarding the different contributions from compression or dilatation occurring during the co-seismic deformation within each layer of the Earth, or those resulting from the radial displacements of the surface and inner interfaces separating layers of different densities, we have decomposed the Poisson equation in order to discriminate between gravitational perturbations due to volume and topography changes, as detailed in [29]. This new mathematical development has allowed us to address the style of deformation, dilatational *versus* compressional ones, without the limitations suffered by plane half-space models, as in [32]. Furthermore, instead of the compressible model used by [35] to quantify the effects of the 2004 Sumatran earthquake on the Earth's rotation, based on [36] analytical approximation of compressibility, as discussed in [10], our model now fully accounts for the effects of compressibility, both in the initial state and during the perturbations [4], as described in the first three sections of this study, on the basis of the Runge-Kutta integration in the radial variable of the differential equations describing the momentum conservation and self-gravitation.

The results from sect. **5** indicate that, thanks to the technological achievements described in sect. **4**, we can nowadays overcome the limitation posed by the possibility of detecting the gravity signals only for earthquakes of magnitudes higher than $M_w = 8.5$. Being such huge earthquakes those occurring at subduction zones within a tectonic environment associated to compression, the new technology and the NGGM give us the opportunity to disclose the new physics herein described for earthquakes with magnitudes as low as $M_w = 7$ and different tectonic environments, such as extensional ones as in southern Italy.

In particular, the new findings of sect. **5** show that at the spatial resolution of GOCE, the NGGM has the capability to resolve not only the co-seismic-gravity signal, but also the post-seismic one. In fact, we have shown that the post-seismic contribution can be as high as 5–8 μGal, for the deep and shallow sources, which makes the detection of the post-seismic contribution feasible, since the expected flight duration of the NGGM is eleven years, representing a span of time during which the total amount of this post-seismic contribution, or at least a major part of it, will be accumulated and thus made visible by the gravity mission.

* * *

The authors thank Andrea Bizzarri and Alessandro Bettini for their invitation to write this article, they thank Maurizio Fedi for having invited one on the authors to give a lecture at the 2017 103° SIF meeting, September 11-15, in Trento on the physics of earthquakes from gravity, without whom this article would not have had the chance

to be written. The authors thank Stefano Cesare and Alberto Anselmi for their contribution to sect. **4** on the Next Generation Gravity Mission. This work is supported by the ESA (European Space Agency) grant "Gravitational Seismology", EO Science For Society, ESA ITT AO/1-9101/17/I-NB, including the Department of Earth Sciences of the University of Milano, Thales Alenia Space - Italy, and the Institute of Geodesy of the University of Stuttgart.

Appendix A.

Spatial resolution

In order to discuss the gravity anomalies caused by earthquakes at the different spatial resolutions of the space gravity missions, we consider the following spatial averages of the perturbation of the gravitational potential:

$$\widehat{\phi}^{\Delta}(r,\theta,\varphi) = \int_{\Omega'} \phi^{\Delta}(r,\theta',\varphi')\, W(\alpha)\, \mathrm{d}\Omega', \tag{A.1}$$

where W is the Jekeli's Gaussian averaging function [28]

$$W(\alpha) = \frac{b}{2\,\pi}\, \frac{e^{-b\,(1-\cos\alpha)}}{1-e^{-2\,b}}\,. \tag{A.2}$$

Here, α is the angle between the (θ,φ) and (θ',φ')

$$\cos\alpha = \cos\theta\cos\theta' + \sin\theta\sin\theta'\cos(\varphi-\varphi') \tag{A.3}$$

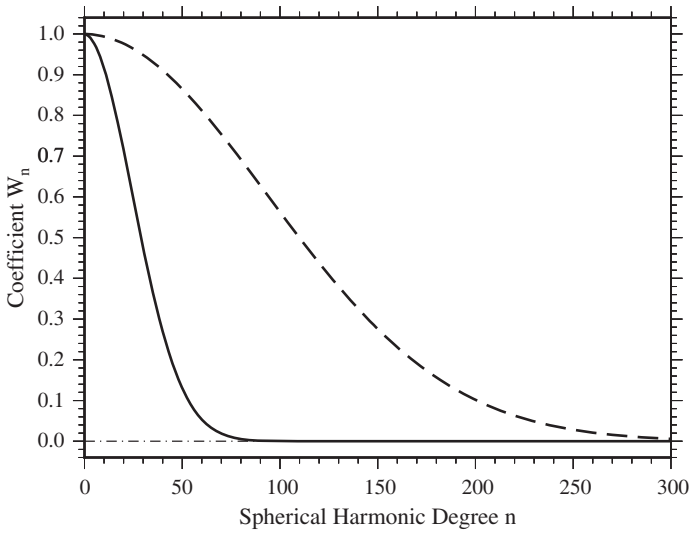

Fig. 18. – Coefficients W_ℓ of the Jekeli's Gaussian filter of radius $R_W = 300$ and 80 km (solid and dashed lines).

and b is a parameter that controls the smoothing process, usually expressed in terms of the distance on the Earth surface, R_W, at which W drops to 1/2 its value at $\alpha = 0$ [37]

$$b = \frac{\ln(2)}{1 - \cos(R_f/a)}\,, \tag{A.4}$$

that is $W(R_W/a) = W(0)/2$.

We note that this spatial average acts as a low-pass filter and has the advantage of compensating the poorly unknown, short-wavelength spherical harmonic coefficients. Indeed, as shown in [28], the spherical harmonic coefficients of the smoothed gravitational potential, $\hat{\Phi}_{\ell m}$, become

$$\widehat{\Phi}_{\ell m} = W_\ell\, \Phi_{\ell m}, \tag{A.5}$$

where the coefficients W_ℓ can be computed with the following recursion relations:

$$\begin{aligned} W_0 &= 1; \\ W_1 &= \coth(-b) - \frac{1}{b}\,; \\ W_\ell &= W_{\ell-2} - \frac{2\,\ell - 1}{b}\, W_{\ell-1}. \end{aligned} \tag{A.6}$$

The gravity anomalies at the GRACE and GOCE spatial resolution discussed in the main text are obtained considering all spherical harmonic coefficients provided by the two missions, up to $\ell = 90$ and 250, respectively, and applying a Jekeli's Gaussian filter with averaging radius of $R_W = 300$ and 80 km, respectively. The coefficients W_ℓ are shown in fig. 18.

REFERENCES

[1] Cesare S., Allasio A., Anselmi A., Dionisio S., Mottini S., Parisch M., Massotti L. and Silvestrin P., *Sci. Direct, Adv. Space Res.*, **57** (2016) 1047.
[2] Sabadini R., Vermeersen B. and Cambiotti G., *Global Dynamics of the Earth - Applications of Viscoelastic Relaxation Theory to Solid-Earth and Planetary Geophysics*, 2nd edition (Springer) 2016.
[3] Wolf D., *Geophys. J. Int.*, **104** (1991) 401.
[4] Cambiotti G. and Sabadini R., *Geophys. J. Int.*, **180** (2010) 475.
[5] Wolf D. and Kaufmann G., *Geophys. J. Int.*, **140** (2000) 51.
[6] Birch F., *Geophys. Res. Lett.*, **57** (1952) 227.
[7] Dziewonski A. M. and Anderson D. L., *J. Geophys. Res.*, **25** (1981) 297.
[8] Ben-Menahem A. and Singh S. J., *Seismic Waves and Sources* (Springer, New York) 1981.
[9] Smylie D. A. and Mansinha L., *Geophys. J. R. Astron. Soc.*, **23** (1971) 329.
[10] Cambiotti G., Barletta V. R. Bordoni A. and Sabadini R., *Geophys. J. Int.*, **176** (2009) 995.
[11] Tanaka Y., Okuno J. and Okubo S., *Geophys. J. Int.*, **164** (2006) 273.
[12] Plag H.-P. and Jüttner H.-U., *J. Geodyn.*, **20** (1995) 267.
[13] Vermeersen L. L. A. and Mitrovica J. X., *Geophys. J. Int.*, **142** (2000) 351.
[14] Fang M. and Hager B. H., *Geophys. J. Int.*, **123** (1995) 849.
[15] Spada G., Sabadini R., Yuen D. A. and Ricard Y., *Geophys. J. Int.*, **109** (1992) 683.
[16] Vermeersen L. L. A. and Sabadini R., *Geophys. J. Int.*, **129** (1997) 531.

[17] Silvestrin P., Aguirre M., Massotti L., Leone B., Cesare S., Kern M. and Haagmans R., *Int. Assoc. Geodesy Symp.*, **136** (2012) 223.
[18] Bender P. L., Wiese D. N. and Nerem R. S., in *Proceedings of the 3rd International Symposium on Formation Flying, Missions and Technologies* (ESA/ESTEC, Noordwijk) 2008, pp. 23–25.
[19] Pour S. I., Reubelt T., Sneeuw N., Daras I., Murbck M., Gruber T., Pail R., Weigelt M., van Dam T., Visser P., de Teixeira da Encarnao J., van den IJssel J., Tonetti S., Cornara S. and Cesare S., *Assessment of Satellite Constellations for Monitoring the Variations in Earth's Gravity Field, Final Report* (ESA Contract 4000108663/13/NL/MV, University of Stuttgart, Institute of Geodesy) 2015.
[20] Pail R., Bingham R., Braitenberg C., Dobslaw H., Eicker A., Güntner A., Horwath M., Ivins E., Longuevergne L., Panet I. and Wouters B., *Surv. Geophys.*, **36** (2015) 743.
[21] Barzaghi R., Marotta A.M., Splendore R. De Gaetani C. and Borghi A., *Geophys. J. Int.*, **197** (2014) 22.
[22] Marotta A. M. and Sabadini R., *Geophys. J. Int.*, **175** (2008) 742.
[23] Jiménez-Munt I., Sabadini R., Gardi A. and Bianco G., *J. Geophys. Res.*, **108** (2003) ETG 2-1.
[24] Dalla Via G., De Natale G., Troise C., Pingue F., Obrizzo F., Riva R. and Sabadini R., *Geophys. J. Int.*, **154** (2003) F9.
[25] Cambiotti G., Ricard Y. and Sabadini R., *Geophys. J. Int.*, **183** (2010) 1248.
[26] Marotta A. M. and Sabadini R., *Geophys. J. Int.*, **157** (2004) 865.
[27] Marotta A. M., Spelta E. and Rizzetto C., *Geophys. J. Int.*, **166** (2006) 923.
[28] Jekeli C., *Alternative methods to smooth the Earth's gravity field, Rep. 327* (Department of Civil and Environmental Engineering and Geodetic Science, Ohio State University, Columbus) 1981.
[29] Cambiotti G., Bordoni A., Sabadini R. and Colli L., *J. Geophys. Res.*, **116** (2011) B10403.
[30] Kusche J., Schmidt R., Petrovic S. and Rietbroek R., *J. Geod.*, **83** (2009) 903.
[31] Tsai V. C., Nettles M., Ekstrom G. and Dziewonski A. M., *Geophys. Res. Lett.*, **32** (2005) L17304.
[32] Han S. C., Shum C. K., Bevis M., Ji C. and Kuo C. Y., *Science*, **313** (2006) 658.
[33] de Linage C., Rivera L., Hinderer J., Boy J. P., Rogister Y., Lambotte S. and Biancale R., *Geophys. J. Int.*, **176** (2009) 695.
[34] Gross R. S. and Chao B. F., *Surv. Geophys.*, **27** (2006) 615.
[35] Sabadini R., Riva R. E. M. and Dalla Via G., *Geophys. J. Int.*, **171** (2007) 231.
[36] Gilbert F. and Backus G., in *Dynamics of Stratified Solids*, edited by G. Herrmann (American Society of Mechanical Engineers, New York) 1968, pp. 82–95.
[37] Wahr J. and Molenaar M., *J. Geophys. Res.*, **103** (1999) 30205.